POLARIZATION-BASED IMAGE SEGMENTATION AND HEIGHT ESTIMATION FOR INTERFEROMETRIC SAR

THESIS

Augusta J. Vande Hey, B.S.Phy., Second Lieutenant, USAF

AFIT-ENG-MS-22-J-016

DEPARTMENT OF THE AIR FORCE
AIR UNIVERSITY

AIR FORCE INSTITUTE OF TECHNOLOGY

Wright-Patterson Air Force Base, Ohio

AFIT-ENG-MS-22-J-016

POLARIZATION-BASED IMAGE SEGMENTATION AND HEIGHT ESTIMATION FOR INTERFEROMETRIC SAR

THESIS

Presented to the Faculty

Department of Electrical and Computer Engineering

Graduate School of Engineering and Management

Air Force Institute of Technology

Air University

Air Education and Training Command

in Partial Fulfillment of the Requirements for the

Degree of Master of Science in Electrical Engineering

Augusta J. Vande Hey, B.S.Phy., B.S.Phy.

Second Lieutenant, USAF

June 16, 2022

AFIT-ENG-MS-22-J-016

POLARIZATION-BASED IMAGE SEGMENTATION AND HEIGHT ESTIMATION FOR INTERFEROMETRIC SAR

THESIS

Augusta J. Vande Hey, B.S.Phy., B.S.Phy.
Second Lieutenant, USAF

Committee Membership:

Julie A. Jackson, Ph.D
Chair

Richard K. Martin, Ph.D
Member

Robert F. Mills, Ph.D
Member

AFIT-ENG-MS-22-J-016

Abstract

To find scatterers in a synthetic aperture radar (SAR) image, a modification is proposed to improve peak region segmentation (PRS) with region merging. The modification considers the polarization of each pixel before it is added to a segment to ensure the segment only contains pixels of the same polarization. Prior to region merging, the polarization of the segments is compared, so that only segments with the same polarization are merged into a single region. The segmented regions are used to find the height of each scatterer through interferometric SAR (IFSAR) processing.

Five methods of IFSAR processing are considered in this thesis. The maximum likelihood (ML) estimate for a single polarization channel is expanded to include data from all four polarization channels. A least squares estimator is also evaluated for both a single pixel per segment and all the pixels in the segment. Both least squares estimators use data from all four polarization channels. The ML and least squares estimators are compared to a pixel-by-pixel IFSAR estimator to determine which provides the most accurate and precise results. The best height results come from using all the pixels in the segment from all four polarization channels.

Table of Contents

List of Figures

List of Tables

POLARIZATION-BASED IMAGE SEGMENTATION AND HEIGHT ESTIMATION FOR INTERFEROMETRIC SAR

I. Introduction

1.1 Problem Background

Synthetic aperture radar (SAR) is a method of radar imaging that moves an antenna along an aperture to simulate a much larger antenna. SAR provides day/night all-weather long range sensing. SAR images can be difficult to interpret compared to elctro-optical images. Without the ability to determine what objects are in a scene and their location, SAR imagery ceases to provide useful information. To make the images meaningful, methods are needed to find the individual objects in the scene and estimate the $x, y, z-$coordinates of each object.

One way to find the objects and their locations is through image segmentation and feature extraction. Image segmentation typically divides the image into regions of similar magnitude. Feature extraction seeks to estimate several parameters of the object including size, shape, orientation, and location. This thesis focuses on finding each object's height or $z-$coordinate in feature extraction and using the polarization of the objects in the scene to improve the image segmentation. The accuracy of the height estimates and the image segments affects how well the scene can be rebuilt.

1.2 Proposed Solutions

To improve the image segmentation, we propose a modified image segmentation algorithm building off the image segmentation algorithm in [1]. The original algorithm

segments the image by comparing the magnitude of each pixel to multiple thresholds [1, 2]. The segments are then merged together to avoid oversegmentation [1]. This thesis modifies the algorithm in [1] to check the polarization of each pixel before it is added to a segment to ensure that each segment only contains one polarization type. Comparing the polarization and magnitude ensures a more accurate single-feature representation in a segment.

This thesis also proposes multiple methods to determine the height of the objects from the segments formed. The least squares method in [2] is recreated and compared to the pixel-by-pixel technique in [2] and the maximum likelihood one in [3]. The maximum likelihood method from [3] is further explained in Section 2.4. Both the least squares and maximum likelihood height estimates are found from a single pixel and multiple pixels from either a single polarization or all four polarizations. The single pixel version of the least squares estimator takes the centroid pixel for each polarization channel and forms them into a 2×2 matrix for each image. The height is determined by the angle between the matrices. To compare the performance of all the methods, we will compute the mean and the variance of each method and use the values to determine which gives the most accurate and precise estimates.

1.3 Thesis Overview

Chapter II provides information on the image segmentation algorithm in [1] and [2], explains relevant details to the methods used in this paper, other methods used, and shows previous works. Chapter III discusses the algorithm modifications proposed for image segmentation and shows the results of the modified algorithm. Chapter IV explains the height estimation methods in detail, provides numerical examples for each method proposed, and analyzes which estimator has the most accurate mean and lowest variance. Finally, Chapter V concludes the thesis.

II. Background and Literature Review

SAR systems overcome some the limitations of electro-optical and infrared systems to produce high quality images of the earth's surface [3]. To understand the images produced by the radars, detection, estimation, and classification are needed. The analysis steps for SAR images are segment the image, estimate the parameters of each scattering center through feature extraction, and classify the target(s) formed by the scattering centers.

Radar images are difficult to interpret, since the image is not a typical electro-optical image where the objects are easily recognized for what they are. Instead radar images show the reflectivity of the electromagnetic (EM) wave from each scattering center [3]. Feature extraction is necessary to determine what objects are contained in a scene. Each object has at least one scattering center and feature extraction seeks to detect and estimate these scattering centers [4]. The extracted features can be used for computer-based target recognition. The detection piece consists of detecting parametric scattering models. Parametric scattering models briefly described in Section 2.5 are used rather than isotropic point scatterers [2, 4, 5]. Parametric scattering models provide more information than isotropic point scatterers, specifically polarimetric information and physical structure [2, 5]. The parametric models include the top-hat, sphere, cylinder, plate, trihedral, and dihedral. The scatterers are found by segmenting the image described in Section 2.3 to find the highest energy regions.

The segmented image is then used to estimate the location and orientation of each of the scatterers. The shape is partially determined by the polarimetric response of the scatterer. The polarimetric response can be classified as odd or even bounce as described in Section 2.2. An odd bounce corresponds to the plate, trihedral, cylinder, or sphere, while an even bounce corresponds to the top-hat or dihedral [2, 4, 5] The estimated shape, location, and orientation information is useful for rebuilding the 3D

scene. The estimated scatterers can be laid over a computer-aided design (CAD) model to help understand what the scene looks like.

2.1 SAR Geometry and Image Collection

Radar systems can have several different configurations, but this thesis assumes a monsostatic radar so that the transmitter and receiver are co-located. The azimuth angle is denoted by ϕ and the elevation angles are denoted by θ_1 and θ_2 and are depicted in Figure 1. Two elevations are used to collect a pair of interferometric SAR (IFSAR) images. The elevation angles or grazing angles are the angle between the ground plane and the aperture's line-of-sight at the halfway point [3]. The elevation angle along with the radar bandwidth determines the range resolution of the image [3] by

$$\rho_r = \frac{c}{2BW \cos\theta} \tag{1}$$

where BW represents the bandwidth and c the speed of light. The azimuth angle is the angle between the radar and the range direction [3]. The aperture extent is the range of azimuth angles the radar uses for the scene and determines the scene extent in the cross-range direction and the cross-range resolution by

$$\rho_{cr} = \frac{\lambda}{4 \sin\left(\frac{\Delta\phi}{2}\right) \cos\left(\theta\right)} \tag{2}$$

where $\Delta\phi$ is the aperture extent and λ is the radar's wavelength [3].

At each given azimuth and elevation angle, the radar transmits an electromagnetic (EM) pulse and receives an echoed signal from the illuminated ground [3]. Each radar pulse projects any objects in the pulse's path into a 2D plane. The information collected from all the pulses forms the complex phase history in each polarization channel, which is the reflectivity of everything illuminated by the radar beam including

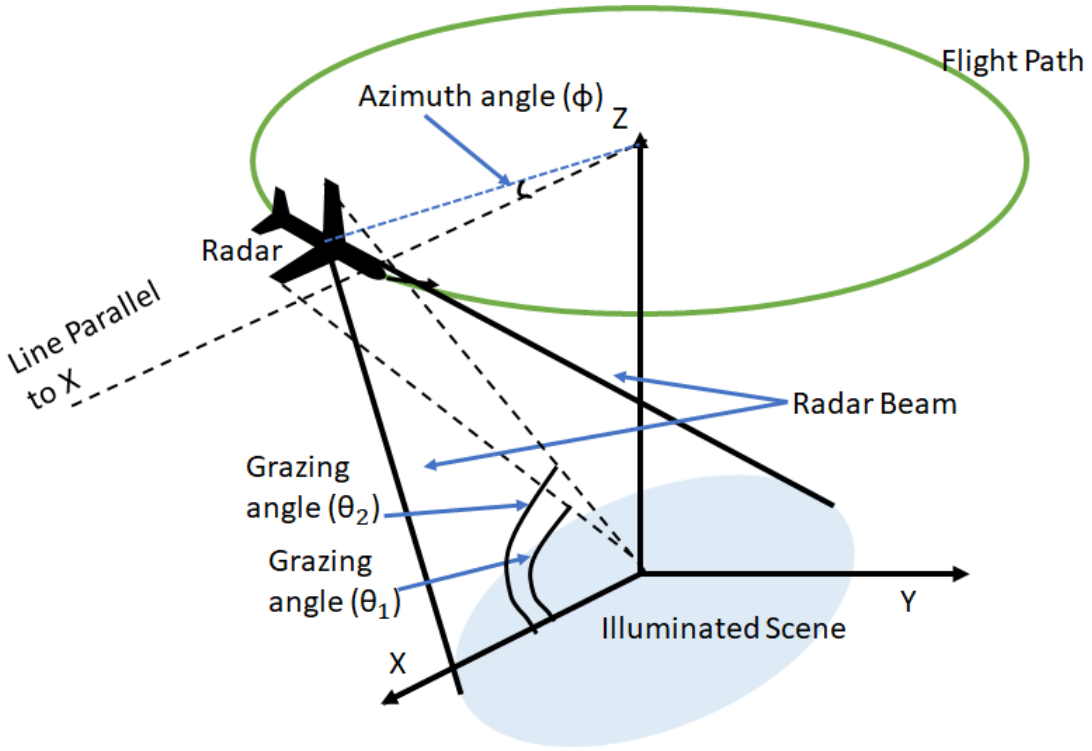

Figure 1: Geometry of a SAR collection for an IFSAR image pair for the monostatic case.

trees, buildings, cars, etc. [3]. The phase history is processed through backprojection, which is used in this thesis, or a polar format algorithm to form the radar images. Each fully polarimetric radar image consists of four images, one from each polarization channel. The IFSAR pair consists of eight images shown in Figures 3a-3f, though only six images are shown since the monostatic case assumes the HV and VH cases are the same. The radar images are of the scene in Figure 2 taken at $\theta_1 = 20°$ and $\theta_2 = 20.05°$ for all four polarization channels.

2.2 Polarimetric Scattering

The images in the previous section can be formed from a single polarization channel or from all four polarization channels. The radar pulses are polarized as vertical or horizontal depending on the orientation of the electric field. When the EM wave

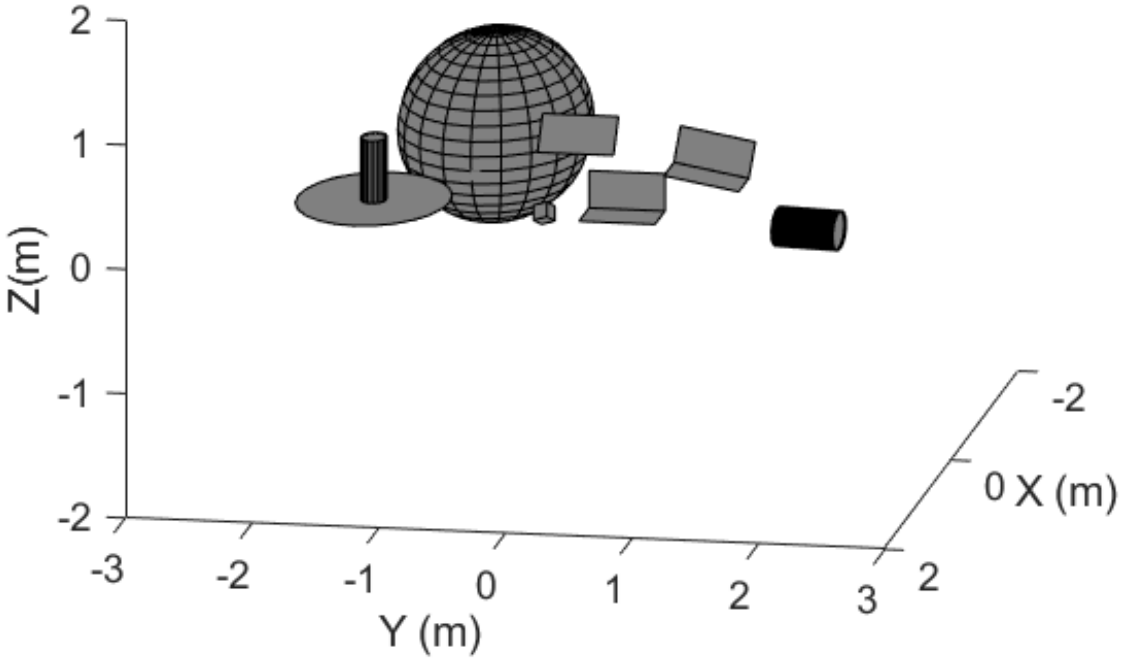

Figure 2: Model of a scene including the top-hat, sphere, cylinder, two dihedrals, and trihedral from [4].

interacts with an object, the EM wave scatters and can change orientation. If the object is isotropic, the EM wave scatters the same regardless of how it hits the scatterer. Conversely, if the object is anisotropic, the EM wave will scatter differently depending on the object's orientation and shape. The effects of anisotropic scattering are further studied in Chapter III.

The images are comprised of several pixels that have their own magnitude and polarization. Each pixel is associated with a scattering matrix, S [6]. Typically, S is a 2×2 matrix

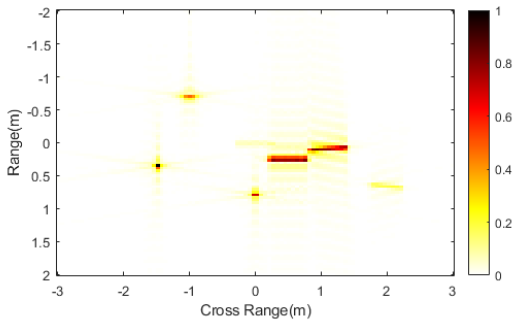

(a) HH, $\theta = 20°$

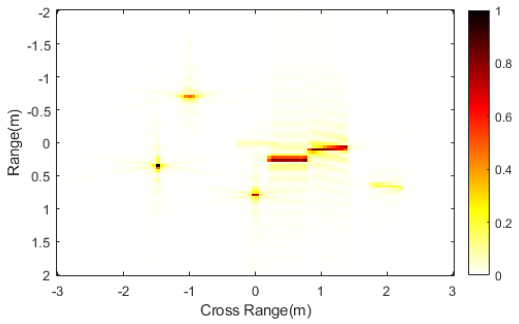

(b) HH, $\theta = 20.05°$

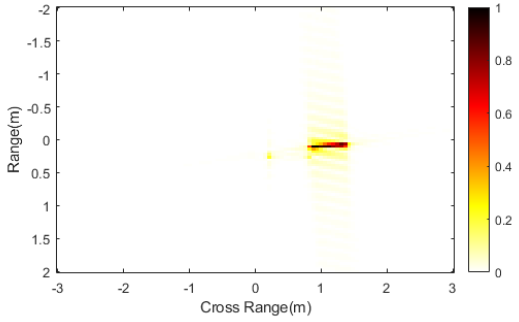

(c) HV=VH, $\theta = 20°$

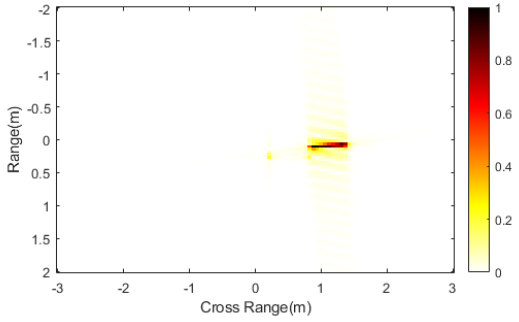

(d) HV=VH, $\theta = 20.05°$

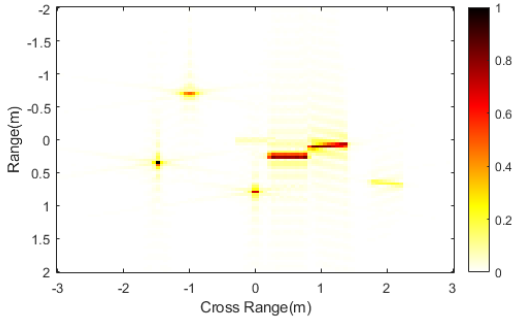

(e) VV, $\theta = 20°$

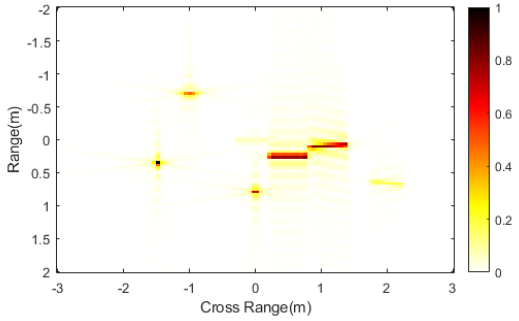

(f) VV, $\theta = 20.05°$

Figure 3: Radar images for each polarization channel at both elevations of the IFSAR image pair collected in Figure 1 of the canonical scene in Figure 2.

$$S = \begin{bmatrix} S_{HH} & S_{HV} \\ S_{VH} & S_{VV} \end{bmatrix} \tag{3}$$

such that the subscripts H and V denote the horizontal or vertical polarization respectively of the transmitter (first subscript) and receiver (second subsript) [6]. For a fully polarimetric image, all four elements of the matrix are present. In the monostatic case, the cross-pol channels, S_{HV} and S_{VH} are assumed to be equal.

The scattering matrix of each pixel shows how the EM wave will be scattered. The EM wave can have an odd bounce or an even bounce depending on how many times the wave hits the object and/or the ground before returning to the radar. Each pixel is characterized by the EM wave's polarimetric response, which can be used to help segment the image as in Chapter III based on the methods in Section 2.3.

The polarimetric response of each pixel is compared to basis vectors so the polarization can be determined as having an odd or even bounce [2]. The basis vectors for the trihedral-dihedral basis are defined as [2]

$$B_{odd} = \begin{bmatrix} 1 \\ 0 \\ 0 \end{bmatrix} \qquad B_{even} = \begin{bmatrix} 0 \\ \cos(2\psi) \\ \sin(2\psi) \end{bmatrix} \qquad B_{cross} = \begin{bmatrix} 0 \\ \sin(2\psi) \\ -\cos(2\psi) \end{bmatrix} \tag{4}$$

where ψ is the rotation angle of the scatterer described in [2]. Only the first two vectors are used in this thesis; however, the third basis vector represents the cross-polarization response and would be used if the dihedral were rotated about the radar line of sight. Other basis vectors that can be used to determine polarization are found in [7]. The basis vectors can be used in a classification scheme to determine what group a scatterer belongs to [2].

2.3 Segmentation

Image segmentation or detection is the first step of feature extraction. Detection involves finding the highest energy regions by segmenting the composite image (Figure 5a) described in Section 2.5.1 [1,2]. The image segmentation can be accomplished with the watershed algorithm; however the watershed algorithm leads to oversegmentation since it segments based on local minima [1]. The watershed algorithm is similar to the geographical watershed. Watershed lines determine which valley water flows into based on where ridge-lines or watershed lines occur. In the case of SAR images, the ridge-lines are represented by pixel magnitudes within the image. Based on the magnitude of the ridge-lines, the pixels are sorted into bins or segments represented by the valleys in the metaphor.

The watershed algorithm is modified and improved in [1, 2] to correct the oversegmentation issue. Jackson uses the inverted watershed algorithm or peak region segmentation (PRS) instead [1, 2]. The inverted watershed algorithm segments the image similar to the watershed algorithm except the peaks rather than the valleys are the highest energy region. The peaks are formed by taking the highest energy pixels in the scene and joining the user-defined neighbors with those pixels. If the pixels are below a set threshold, τ_3, they are not considered at all [1]. The resulting images, Figures 4a and 4b, are oversegmented due to ripple effects, but typically also due to noise and clutter. To solve the oversegmentation, each peak can be merged with other peaks that are within a certain threshold,τ_1, of the first peak [1, 2]. The algorithm from [1, 2] continues until all eligible peaks are merged shown in Figures 4c and 4d. Once the peaks are formed any pixels that are below a third threshold τ_2 are removed from the image [1].After the peaks are merged, [1] removes the highest energy scatterers from the scene first. Removing the highest energy regions first makes finding low energy scatterers easier. We assume that each region corresponds

to a single scatterer.

The algorithm can also be applied to a 2D case, which has the same oversegmentation issue in Figure 5b. The region merging again solves the issues (Figure 5c) so that the segmented image has the same number of segments as the original scene (Figure 2) and the composite image (Figure 5a).

While the modified algorithm in [1, 2] removes the oversegmentation problem, it does still have limitations. The issue with the algorithm is that it only depends on the magnitude of the pixels. If scatterers from different objects are too close together, the algorithm cannot tell them apart and segments them as a single scatterer. When feature extraction is applied to the segmented image, some objects are mis-classified as being a part of a different object. The mis-classification issue can be solved by comparing the polarimetric information of each pixel as well as its magnitude. For example, if the polarization were to change partway through the first segment in Figure 4b, the segmenter would still include them in a single segment even though the segment should be split in two.

2.4 IFSAR Processing

The image segments formed in the previous section can be used to find the $x, y, z-$ coordinate. SAR imaging projects a 3D scene into a 2D image, so the z coordinate lays over to the corresponding range bin in the images. In order to understand the imaged scene, the 3D scene must be reconstructed from the 2D image. One method of recovery is to obtain enough passes of the scene to obtain Nyquist sampling in the vertical direction where each pass has an increased elevation from the previous. While theoretically possible, this method of recovery requires very narrow spacing between passes, is extremely slow, and is computationally burdensome.

A more practical method is interferometric SAR (IFSAR) processing. IFSAR

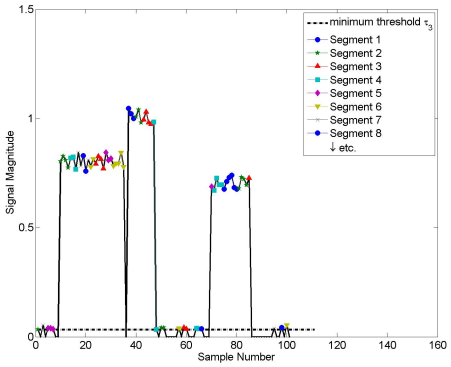

(a) Segmentation without Region Merging

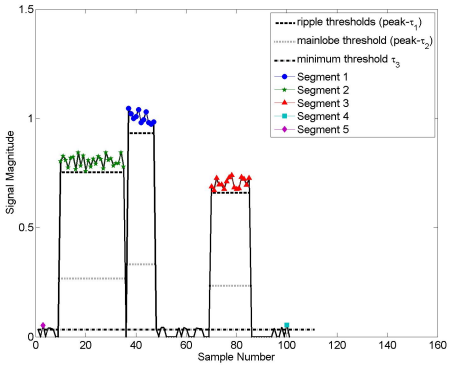

(b) Segmentation with Region Merging

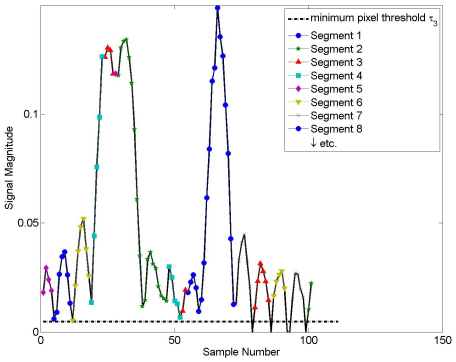

(c) Segmentation without Region Merging for a Localized Case

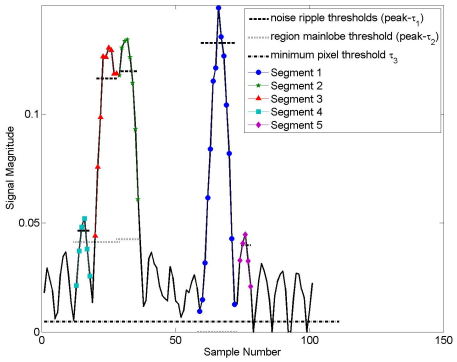

(d) Segmentation with Region Merging for a Localized Case

Figure 4: Examples showing a 1D case segmented with the inverted watershed algorithm with and without region merging [1].

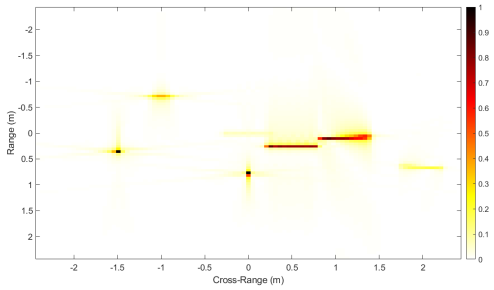

(a) Composite Image

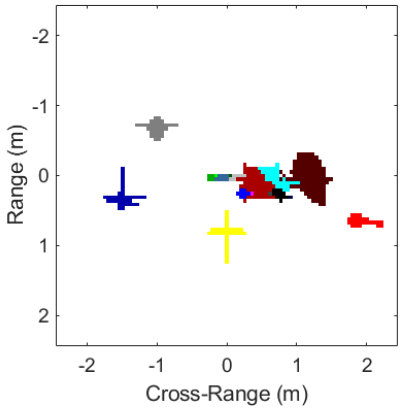

(b) Initial Segmentation

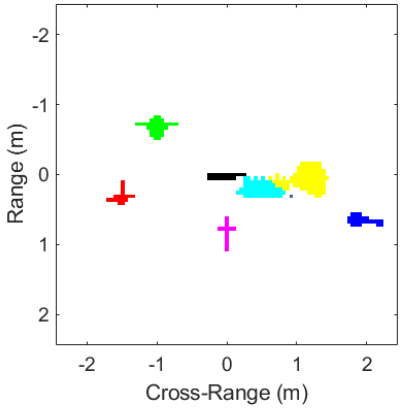

(c) Final Segmentation

Figure 5: Composite image of the scene including the top-hat, sphere, cylinder, two dihedrals, and trihedral from [4] and shown in Figure 2. The models are segmented image using an inverse watershed method where each color represents a new segment. Region merging is then applied to reduce the number of segments with $\tau_1 = -1$ dB, $\tau_2 = -25$ dB, and $\tau_3 = -35$ dB.

interferes at least two images of the same scene that are spaced temporally and/or spatially [3]. While a minimum of two images are required, eight images are used throughout this thesis. The two images can be collected in one pass by a radar system with two antennas or in multiple passes [3]. If images come from multiple passes, the reflectivity function of the terrain, $r(x, y)$, can temporally change or the aperture region support, A_1 and A_2, can change between passes [3]. However, for single pass radars, neither the reflectivity function nor the aperture changes between the images [3]. Whether the images come from a single pass or a multi-pass, the images have to have some differences for IFSAR processing to work.

One way the images can differ is by a small difference in elevation angles [3]. The image equations depend on the height of the terrain and the elevation angle; the height can be recoved from the phase difference between the images [3]. Let $h(x, y)$ be the terrain height (or scattering object z-coordinate) for reflectivity function $r(x, y, z)$. Assuming only one scatterer per z, the 2D reflectivity $r(x, y)$ is mapped to a SAR image f by

$$f(x_1, y_1) = s_{A_1}(x, y) \otimes [r(x, y) \exp(-j\beta_1 Y_0 h(x, y)) \exp(-jyY_0)] \tag{5}$$

where $\beta_1 = \tan\theta_1$ and $s_{A_i}(x, y)$ is the sinc function from the inverse Fourier transform and Y_0 is the spatial-frequency offset given by [3]

$$Y_0 = \frac{4\pi}{\lambda} \cos\theta \tag{6}$$

which is assumed to be the same for both images [3]. Similarly, the second image (taken from a slightly different elevation angle such that z-coordinate layover in range

does not change positions) can be modeled as

$$g(x_2, y_2) = s_{A_2}(x, y) \otimes [r(x, y) \exp(-j\beta_1 Y_0 h(x, y)) \exp(j(\beta_1 - \beta_2) Y_0 h(x, y)) \exp(-jyY_0)] \tag{7}$$

where $\beta_2 = \tan\theta_2$ [3]. Since the height function is assumed to change slowly and the elevation angle is small enough that the exponential term is considered constant, the phase difference between the images is

$$\Psi = (\beta_1 - \beta_2) Y_0 h(x, y). \tag{8}$$

The equation above implies that the height and phase difference are linearly dependent on each other. The height can then be determined if the phase difference is known, which comes from interfering the images f and g [3].

In [3], Jakowatz explains the process for terrain-height mapping includes image registration, parameter estimation, phase unwrapping, scaling, and orthorectification. To simplify this process, the phase unwrapping step can be removed provided the height falls within a maximum value defined as

$$h_{max} = \frac{c\pi}{4\pi f_c |\tan\theta_1 - \tan\theta_2|} \tag{9}$$

where θ_1 and θ_2 are the elevation angles from each pass shown in Figure 1.

If no scatterer in the scene has a height greater than h_{max}, the phase difference between images f and g is found through parameter estimation [3]. The parameter estimation in [3] looks for the maximum likelihood (ML) estimate of the phase difference between the first image, f, and the second image, g. The ML estimate is

determined by the complex conjugate, f^*g and given by [3]

$$\hat{\Psi}_{ML} = \angle\left(\sum_{k=1}^{N} f_k^* g_k\right). \tag{10}$$

The phase difference given by the ML parameter estimation is used to find the height, since the phase difference is linearly dependent on the height [3]. The height is given by

$$h\left(x,y\right) = \frac{\lambda}{4\pi}\frac{\cos\theta}{\Delta\theta}\Psi\left(x_1,y_1\right) \tag{11}$$

as a function of the elevation, wavelength, and the continuous phase function of the unwrapped phase difference, $\Psi\left(x_1,y_1\right)$ [3].

Besides the ML estimate from [3], there are two ISFAR methods given in [2]. The pixel-by-pixel method compares the phase of the pixels in the first image, f, to the phase of the corresponding pixels of image g [2]. The pixel-by-pixel method also relies on ML estimation, but through single pixel pairs instead of multiple pixels. The comparison is accomplished through conjugate multiplying f and g [2]. Similar to [3], conjugate multiplying the two images makes the height function linearly dependent on the phase. The height is then solved to be

$$h\left(x,y\right) = \Psi\frac{c}{4\pi f_c\left(\tan\theta_1 - \tan\theta_2\right)\cos\left(\frac{1}{2}\left(\theta_1+\theta_2\right)\right)} \tag{12}$$

where Ψ is the phase function similar to Equation (11) and defined by $\Psi = \angle f^*g$ for individual pixel pairs [2] and the height function is normal to the slant plane and related to the z-coordinate in [2] by

$$z = H\cos\bar{\theta}. \tag{13}$$

The second method, proposed in [2], is to find the least squares solution of the

phase difference, Ψ, between the two passes. This method is further explained in Section 4.2.2. The phase difference is estimated with least squares, since the resulting height estimates would have a lower variance [2]. The main difference between the least square estimate in [2] and the ML estimate from [3] is that the least squares method uses the data from all four polarization channels [2] rather than just one polarization channel [3].

The height estimates above assume the images are registered prior to IFSAR processing. To register the two images, one image must be interpolated so that any given scatterer has the same indices in both images [3]. In this thesis, small elevation angle differences between the two images are used to ensure the image pairs are registered without additional processing. Once the images are registered, IFSAR processing can estimate the phase difference through parameter estimation.

The remaining steps of scaling and orthorectification are to remove the scale factor of Y_0 and to remove the layover effects, which are a result of a 3D scene projected onto a 2D image. The layover effects are removed by relating the image coordinates x_i and y_i to physical coordinates x, y, and z shown by

$$x = x_i - h\left(x, y\right) \tan\left(\theta\right) \cos\left(\phi\right) \tag{14}$$

$$y = y_i - h\left(x, y\right) \tan\left(\theta\right) \sin\left(\phi\right). \tag{15}$$

Traditionally, IFSAR processing assumes that each resolution cell contains at most one scatterer. The same assumption is made here rather than assuming multiple scatterers per resolution cell as in [8].

2.5 Overview of the Feature Extraction Algorithm

The previous sections describe steps involved in feature extraction, which is the process of detecting and classifying the scatterers in a scene. An algorithm for feature extraction is presented in [2]. A summary of the key steps in Jackson's algorithm is shown in Table 1 given two images, f and g. In [2], the algorithm is tested on parametric scattering models. The parametric scattering models or canonical models consist of the top-hat, plate, sphere, cylinder, dihedral, and trihedral, which are shown are Figure 2. The shapes are formed through combinations of 2D planar models such as the flat plate, right angle, and circular surface [5]. A comprehensive explanation of the parametric models and their mathematical equations can be found in [5].

The algorithm in [2] is explained in the subsequent subsections using the segmentation and IFSAR processes described in the previous sections or a variation of them. Proposed modifications made to the image segmentation and IFSAR processing steps are described in Chapter III and Chapter IV.

Table 1: Overview of the Feature Extraction Algorithm from [2]

1.	Form two sets of full-polarization images, f and g, from slightly offset elevation angles
2.	Form composite image, C, from f and g using Equation (16) in Section 2.5.1.
3.	Segment composite image using the inverse watershed transform to obtain the pixels in each scatterer as described in Section 2.3.
4.	Classify and estimate canonical scattering features from each segment to include shape and location parameter estimates.
5.	Augment canonical shapes' parameter estimates with z-coordinate or height estimate from IFSAR processing from Section 2.4.

2.5.1 Composite Image

The composite image, C is formed from the fully polarimetric images f and g. Each fully polarimetric image consists of an image from each polarization channel

resulting in eight total images. The composite image is formed by

$$C = \left(|f_{HH}|^2 + |f_{HV}|^2 + |f_{VH}|^2 + |f_{VV}|^2 + |g_{HH}|^2 + |g_{HV}|^2 + |g_{VH}|^2 + |g_{VV}|^2\right)^{\frac{1}{2}} \quad (16)$$

where f_{HH}, f_{HV}, f_{VH}, f_{VV}, g_{HH}, g_{HV}, g_{VH}, g_{VV} are the images formed in each polarization channel. The composite image takes all the polarizations into account and combines them into one image to be segmented as shown in Figure 6, which is the normalized composite image of a simple scene of canonical models shown in Figure 2.

2.5.2 Parameter Estimate Initialization and Classification of Scatterer Type

The segments formed in Section 2.3 are used to estimate the location and type of scatterer. The location estimates are found by finding the average row and column in each segment. Then [2] determines the x and y location of the scatterer from the row

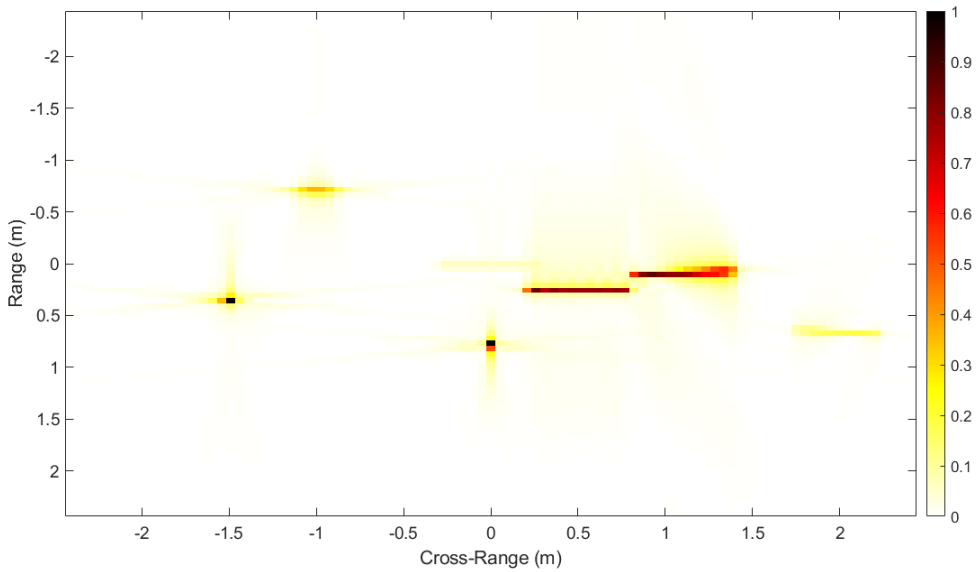

Figure 6: Composite image of the fully polarized canonical scene in Figure 2.

and column pair based on the number of pixels per resolution cell and the image's coordinate system. The x and y estimates, $\tilde{x}$ and $\tilde{y}$, are the coordinates of the 3D object projected into the 2D image plane such that

$$\tilde{x}_m = x_m - z_m \sin\bar{\theta} \tag{17}$$

$$\tilde{y}_m = y_m \tag{18}$$

where the subscript m denotes the m^{th} scatterer, $\bar{\theta}$ is the average of the elevation angles, and x_m, y_m, and z_m are the x, y, z coordinates [2]. From Equation (**??**), the scatterers are assumed to have no layover in the cross-range or y direction, since the radar is assumed to fly along the y-axis.

The length of the scatterer, L_m, is also determined from the segmentation. The length is classified as either distributed or localized. If the scatterer is localized, $L_m = 0$; however, if the scatterer is distributed, then $L_m > 0$ [2]. Distributed scatterers are classified as dihedrals or cylinders, while trihedral or top-hats are classified as localized [2]. The length of the scatterer also changes when the scatterer is projected to the 2D image plane

$$\tilde{l}_m = L_m \cos\psi_m \cos\phi_m \tag{19}$$

where ψ_m is the roll of the object, ϕ_m is yaw, and θ_m is pitch [2].

Between determining if the length is localized or distributed and the polarization decision of the scatterers, [2] also estimates the shape of the scatterer as one of the canonical shapes. An even bounce scatterer corresponds to the dihedral or top-hat. Odd-bounce scatterers correspond to the trihedral, cylinder, sphere, or flat plate [2]. The top-hat, dihedral, trihedral, and cylinder will be examined here.

These estimates give the effective 2D parameters of the 3D scene such that $\Theta_{2D} = \left\{\tilde{x}_m, \tilde{y}_m, \phi_m, \tilde{l}_m, \alpha_m\right\}$ [2]. The value for α_m is either 1 for flat surfaces or $\frac{1}{2}$ for singly-

curved surfaces [2].

The estimated parameters are used to build a model of the scene, whose phase history is contained in the vector $M(\Theta_{2D})$ [2]. The parameters for $M(\Theta_{2D})$ are computed to minimize the least squares between the modeled data and the measured data [2]. Complete details of how the modeled scene is simulated are found in [2]. In [2], all the steps summarized in Table 1 are used to to determine a possible shape type or class and set up initial models. This thesis assumes the shapes are known and will only focus on improving the segmentation and analyze the impact of improved segmentation on IFSAR height estimation.

2.6 Image Segmentation by Polarization

In 2022, a similar concept to that proposed in Chapter III was presented in [9]. The ideas expressed seek to segment images not only by magnitude, but also by polarization. However the methods in [9] differ from the methods proposed in Chapter III. In [9], they propose a two-step process. Similar to Chapter III, the first step is to use a watershed algorithm for the initial segmentation. In contrast, [9] does not use an inverted watershed algorithm. The regions are then merged by a cost function using dual channel polarization, gray tone, texture, and shape features [9]. Similar to this thesis, the method in [9] takes into account how many pixels are in the objects being merged, the length of the objects, and the length of the edge of the bounding boxes. However, [9] only uses the VV and VH channels rather than data from all four polarization channels.

Other methods proposed for segmenting images by polarization are in [10–19]. The methods in [10, 11] involve edge penalties and region statistics. The regions assume either a Wishart or complex Gaussian distribution [10]. In [13], the idea is to use texture features of the image to segment the image into regions. In [14], various

methods of polarized image segmentation are mentioned including Markov random fields [15, 16] and conditional random fields [17, 18]. However, [14] proposes a different method involving semantic segmentation [17] and enhances it with random region matting. Ersahin *et al.* proposes spectral graph partitioning [19]. Spectral graph partitioning combines regions in a pairwise grouping based on a flexible combination of features [19]. Finally, Cloude and Papthanassiou generate interferograms between all combinations of polarization channels and extract the height differences between them [12]. They use coherence optimization to determine the best polarimetric representation and height estimates [12].

III. Polarimetric Image Segmentation

3.1 Image Segmentation Methodology

In contrast to the magnitude segmentation in Section 2.6, the polarization of the pixels is considered prior to the magnitude segmentation from [1]. The pixels can only be segmented with pixels of the same polarization. Once the polarization decision is made, the pixels are segmented by magnitude using Algorithm 1.

In Section 2.6, the segments were formed by looking at each pixel's magnitude in the image and comparing that pixel to its neighbors' magnitude. The neighbors are user-defined as the p pixels away from the pixel in question. The algorithm from [1] is shown in Algorithm 1. We modify the watershed algorithm in [1, 2] to segment the image by polarization as well as magnitude as shown in Algorithm 2.

The polarization of each pixel is given by the original 2×2 scattering matrix [6] described in Section 2.2 and is vectorized and reduced to a 3×1 vector [2]. Since the radar is monostatic, the cross-polarizations, HV and VH, are equivalent [2]. The scattering amplitudes vector of each scatterer,

$$\bar{A} \triangleq \begin{bmatrix} S_{HH} & S_{VH/HV} & S_{VV} \end{bmatrix}^T \tag{20}$$

is compared to each vector B from Section 2.2and the least-squares distance is calculated between $\bar{A}$ and B [2] to determine the scatterer's polarization.

If only the trihedral-dihedral basis from Section 2.2 is used, each pixel in the scatterer is assigned a value of 1 or 2 depending on which basis it has the least distance to [2]. The numbers assigned indicate 1 for the trihedral basis or odd bounce and 2 for the dihedral basis or even basis. Other values can be assigned to the pixels depending on the basis used. Once the pixels are classified by polarization,

the image segmentation algorithm is applied to group the pixels according to their magnitude and polarization. The magnitude of each region and the lowest magnitude considered come from user-defined thresholds [1]. Pixels with magnitudes below the lowest threshold are set to zero for the sake of simplicity. The remaining pixels are then segmented with either Algorithm 2. Algorithm 2 checks that the magnitude of each pixel is within the segment's threshold after ensuring that each pixel in the segment has the same polarization.

Merely segmenting the pixels with the modified inverse watershed algorithm would lead to the oversegmentation issues from Section 2.3 and [1]. Thus, Algorithm 2 includes the region merging from Section 2.3, [1]. However, the region merging step differs slightly from the threshold solution given in [1]. Instead Algorithm 2 merges the regions within the user-defined threshold only if the regions in question have the same polarization. The polarization is checked first so that only pixels with the same polarization are tested for magnitude. In [2], the order is reversed and polarization is only considered in the 3D case after segmentation, so the segments may not consist of a single polarization.

Comparing the polarization of pixels and regions allows us to distinguish objects that are too close together but differ in polarization. In radar images, objects that are too close together are considered unresolvable and cannot be distinguished from each other. Objects can be unresolved in range, cross-range, or both. To determine if objects are far enough apart to be resolved, Equations (1) and (2) are used. Without the modifications, the algorithm takes two pixels or regions with similar magnitudes and assigns them to a single segment. With the modifications, the pixels or regions are not necessarily assigned to the same segment unless they have the same polarimetric properties. For example, a trihedral and dihedral that are unresolved could be segmented separately shown in Section 3.2, which leads to a more accurate repre-

sentation of the scene. Also, distinguishing between two targets is necessary for both the height estimation in Chapter IV and the feature extraction algorithm discussed in Chapter II.

3.2 Image Segmentation Results

Using the same canonical scene as previously (Figure 2) and shown again in Figure 7a, the initial and final segmentation of the image are shown in Figures 7c and 7d using Algorithm 1 in [2]. Figures 7c and 7d using Algorithm 1 are compared to Figures 7e and 7f, which use Algorithm 2. Both algorithms produce the same segmented image, since all the targets are resolvable and the polarization is the same within each scatterer. In the case above, checking the polarization has no impact on how the image segments, since all objects in the scene are resolvable.

In order to demonstrate the usefulness of the polarimetric information, we create and segment six simple scenes with dihedrals and trihedrals. The dihedral and trihedral are chosen, since the dihedral has an even bounce while the trihedral has an odd bounce. The first scene consists of a trihedral and dihedral not resolved in range (Figure 8a). The second scene has a trihedral and dihedral unresolved in cross-range (Figure 9a). The third and fourth scenes have a trihedral and dihedral unresolved in both range and cross-range (Figures 10a and 11a). The fifth image has two dihedrals unresolved in range and cross-range (Figure 12a). Finally, the fourth image has two trihedrals unresolved in range and cross-range (Figure 13a). For all cases, we segmented the image with only magnitude (Figures 8c, 9c, 10c, 11c, 12c and 13c), polarization and magnitude (Figures 8d, 9d, 10d, 11d, 12d and 13d), and polarization (Figures 8e, 9e, 10e, 11e, 12e and 13e). For all cases, elevation $\theta = 20°$, azimuth $\phi = [-8.4°, 8.4°]$, bandwidth is 3 GHz, center frequency is 10 GHz, and resolution is $\rho_r = \rho_{cr} = 0.0508$ m. The dihedral for all cases is 0.6 m long and 0.3 m in height.

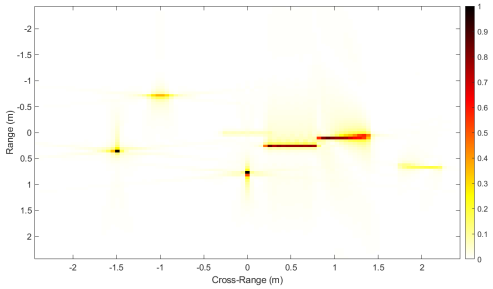

(a) Composite image of Figure 2

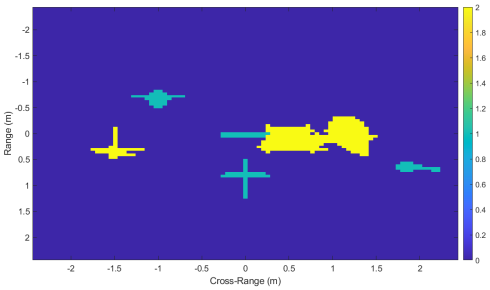

(b) Polarization of the pixels

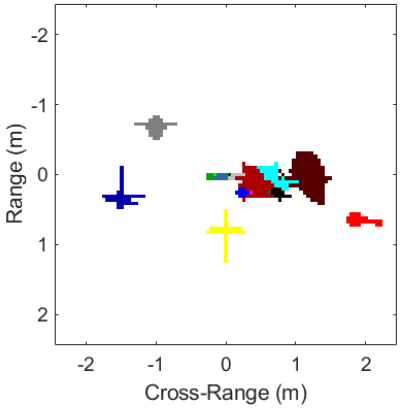

(c) Initial segmentation from Algorithm 1

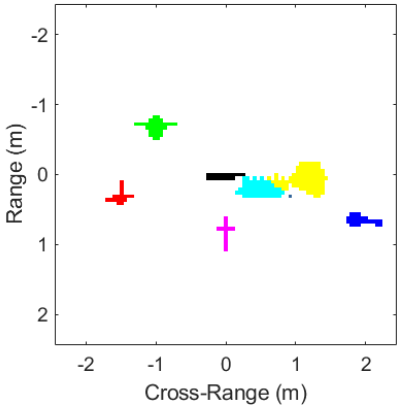

(d) Final segmentation from Algorithm 1

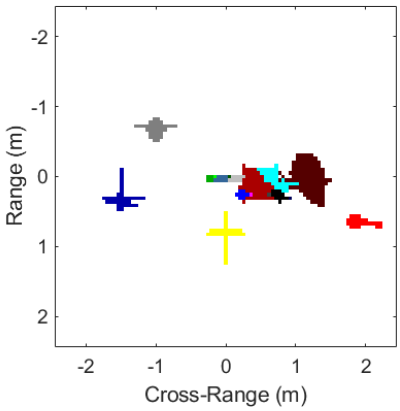

(e) Initial segmentation from Algorithm 2

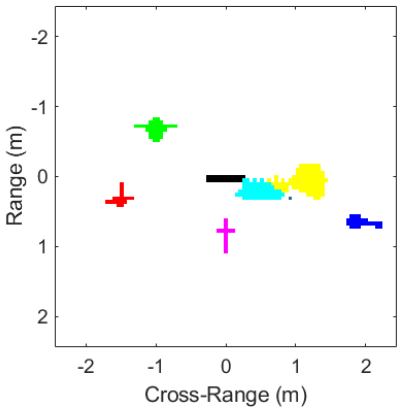

(f) Final segmentation from Algorithm 2

Figure 7: Canonical scene in Figure 2 segmented by both image segmentation algorithms. The segmentation before and after region merging are included as well as the polarization decision for the scene.

Algorithm 1 Magnitude Segmentation Algorithm from [1]

{Peak Region Segmentation}
$P_i \leftarrow$ Sort pixels' magnitudes from high to low (cut off at τ_3)
$l \leftarrow 0$ {Initialize Region Counter}
for $i = n$ to N **do** {Assign Region Labels L_i to each Pixel}
    Consider neighbors of pixel i that are p pixels away in each direction
    if Pixel i has no labeled neighbors **then**
        $l \leftarrow l + 1$
        Assign pixel i a new region label $L_i = l$
    else if ALL labeled neighbors have label L_i **then**
        Assign pixel i to the same region: $L_i \leftarrow L_l$
    else{Labeled neighbors have different labels}
        Assign pixel i to have same label as largest-magnitude neighbor
    end if
end for
{Merge adjacent regions whose nearest pixels have amplitudes within τ_1}
$r = 1$ Initialize region counter
while $r \leq$max number regions **do**
    repeat $threshold \leftarrow$ (peak pixel magnitude in region r)$-\tau_1$
        for $m = 1$ to # regions adjacent to region r **do**
            $dist \leftarrow$ sorted distance of pixels in region m to peak pixel in region r
            $mag \leftarrow$ corresponding magnitude of pixels in region m
            if for $i < j$, $mag(i) < threshold$, and $mag(j) > threshold$ **then**
                Do NOT merge regions
            else
                Re-assign region m pixels to region r
            end if
            {Clip pixels more than τ_2 below region peaks}
            for $i = 1$ to number of pixels in region r **do**
                if Amplitude of pixel $i <$ (Region Peak $- \tau_2$) **then**
                    Re-assign pixel i to region 0
                end if
            end for
        end for
    until No more regions adjacent to region r
    increment region counter: $r \leftarrow r + 1$
end while
Re-order numbering of regions from largest to smallest energy contribution
Re-assign regions with region numbers$>$ max # of desired segments to region 0

The trihedral's height is 0.3834 m and is determined such that it has the same radar cross section (RCS) as the dihedral. The SAR image is formed such that one pixel

Algorithm 2 Polarization Modifications to the Magnitude Segmentation Algorithm

```
{Peak Region Segmentation}
P_i ← Sort pixels' magnitudes from high to low (cut off at τ_3)
Determine polarization of all pixels above τ_3
l ← 0 {Initialize Region Counter}
for i = n to N do {Assign Region Labels L_i to each Pixel}
    Consider neighbors of pixel i that are p pixels away in each direction
    for k = 1 to number of neighbors do
        if pixel i has same polarization as neighbor k then
            pixel i can be segmented with neighbor k
        else
            pixel i cannot be segmented with neighbor k
        end if
    end for
    Do Algorithm 1 until region merging
end for
{Merge adjacent regions whose nearest pixels have amplitudes within τ_1}
r = 1 Initialize region counter
while r ≤max number regions do
    repeat threshold ← (peak pixel magnitude in region r)−τ_1
        for m = 1 to # regions adjacent to region r do
            if polarization of region m = polarization of region r then
                Do Algorithm 1 region merging
            else
                Do NOT merge regions
            end if
        end for
```

corresponds to one radar resolution cell. The roll, pitch, and yaw of the trihedral and dihedral are set to 0°. The remaining parameters for each case are included in Table 2. Finally, the segmentation thresholds are set to $\tau_1 = -4$ dB, $\tau_2 = -25$ dB, $\tau_3 = -35$ dB, and $p = 1$.

Table 2: Parameters for the Six Segmentation Cases

case	shape	x (m)	y (m)	z (m)	Resolved in Range	Resolved in Cross-Range
1	Dihedral	0.25	0.5	0	No	Yes
	Trihedral	0.28	-0.5	0	–	–
2	Dihedral	0.25	0.5	0	Yes	No
	Trihedral	-0.5	0.53	0	–	–
3	Dihedral	0.25	0.5	0	No	No
	Trihedral	0.3	0.3	0	–	–
4	Dihedral	0.25	0.5	0	No	No
	Trihedral	0.27	0.4	0	–	–
5	Dihedral	0.25	0.5	0	No	No
	Diheddral	0.28	0	0	–	–
6	Trihedral	0.25	0.5	0	No	No
	Trihedral	0.3	0.55	0	–	–

In the first case where the dihedral and trihedral are only unresolved in range (Figure 8a), Algorithm 1 segments the two objects separately even with the region merging from [1] (Figure 8c). Adding in the polarization decision does not change the segmentation so Figures 8c and 8d show the same result. The trihedral and dihedral should be kept separate in Algorithm 2, since they do not have the same polarization (Figure 8e). Figure 8d demonstrates that Algorithm 2 also correctly separates the segments for the trihedral and dihedral. Even though the segments are unresolved in range, the composite image in Figure 8b shows that the objects have enough spacing to be segmented separately. The segmented images in Figures 8c

and 8d are compared to Figure 8e, which shows how the image would segment only looking at the polarization of the objects. In case 1, segmenting the image by only magnitude, polarization and magnitude, or only polarization returns the same result.

Similar to the first case, the second case has the same results for Algorithm 1 as for Algorithm 2, (Figures 9c and 9d). In the second case, the dihedral and trihedral are only unresolved in cross-range. Figure 9a shows the two objects in the scene and Figure 9b shows the objects from the radar's perspective. Algorithm 1 segments the image according to Figure 9c. Once again the two objects are in separate segments. Figure 9d demonstrates that Algorithm 2 gives the same results as Algorithm 1 as it should. In the case that a single object has multiple segments due to magnitude differences, Algorithm 2 would maintain the same segments as Algorithm 1. Figure 9e shows how the image would segment if only polarization were considered. Segmenting only by polarization results in a single segment for the dihedral and a single segment for the trihedral. Combining the polarization result with the magnitude decision in Figure 9c gives the same results as Algorithm 1 shown in Figure 9d.

In the third and fourth cases, the trihedral and dihedral are unresolved in both range and cross-range. Figures 10a and 11a show the objects in case 3 and case 4 respectively. The objects are close together, but can still be distinguished in the electro-optical images. Figures 10b and 11b show the radar images for case 3 and 4. Figures 10b and 11b demonstrate that the objects are harder to distinguish from each other in case 3 and cannot be distinguished in case 4. Figure 10c depicts case 3 and segments the image only by magnitude and includes the trihedral as a segment of the dihedral, while Figure 11c shows case 4. The trihedral and dihedral are closer together in case 4, so the mainlobes of the trihedral and dihedral are not distinguishable (Figure 11b). Case 3 has the two objects barely resolved, so the dihedral can somewhat be distinguished from the trihedral (Figure 10b).

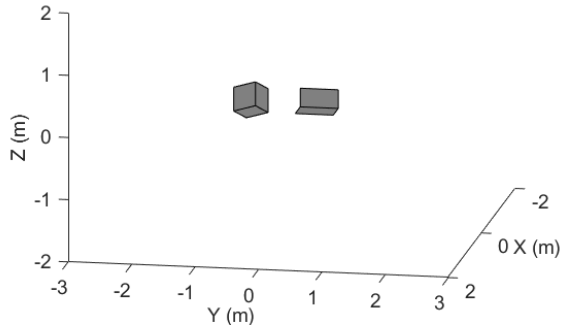

(a) Original scene

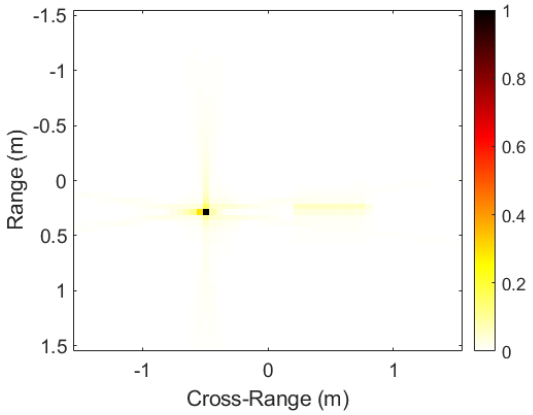

(b) Composite Image

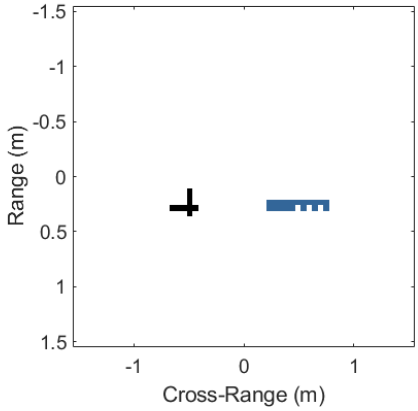

(c) Segmentation by magnitude

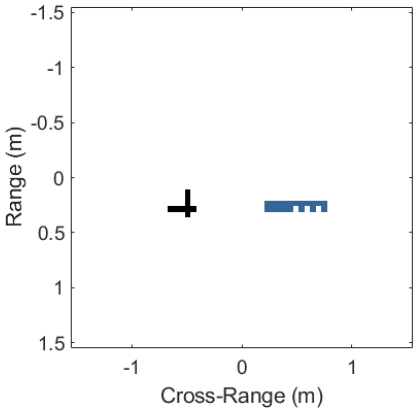

(d) Segmentation by polarization and magnitude

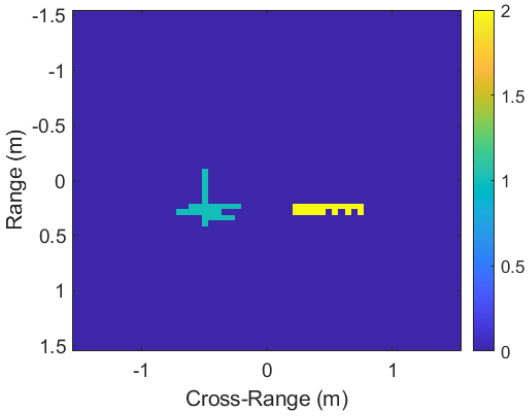

(e) Segmentation by polarization

Figure 8: Case 1 consists of a dihedral and a trihedral unresolved in range. The scene, the composite SAR image for two full-pol passes, the polarization classification, and the segmentations by Algorithms 1 and 2 are shown.

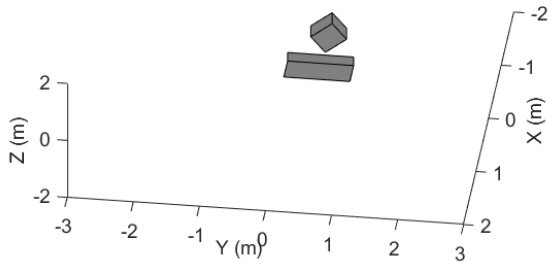

(a) Original scene

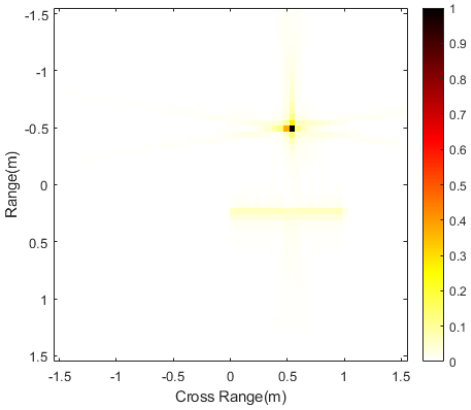

(b) Composite Image

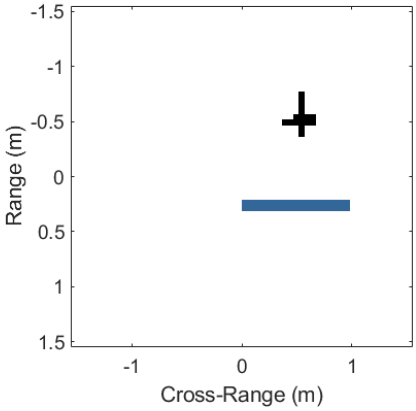

(c) Segmentation by magnitude

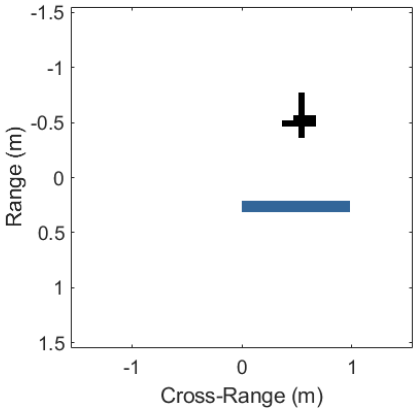

(d) Segmentation by polarization and magnitude

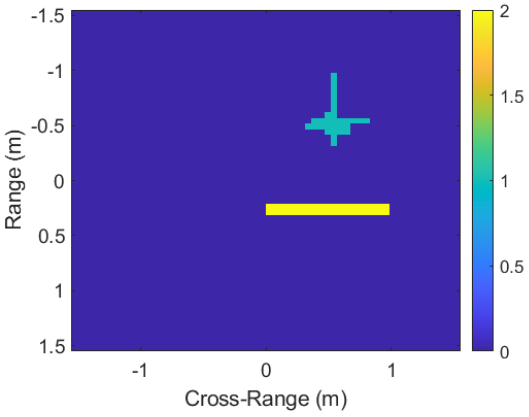

(e) Segmentation by polarization

Figure 9: Case 2 is a simple scene of a dihedral and a trihedral unresolved in cross-range. The scene, the composite SAR image for two full-pol passes, the polarization classification, and the segmentations by Algorithms 1 and 2 are shown.

With the inclusion of polarization, the pixels can be compared and better segmented according to their properties. Figures 10e and 11e give the results if the images are segmented only by polarization. The segmented image has each object in its own distinct segment. However, segmenting only by polarization loses the information of which regions have more energy than others. To get the most accurate representation of the scene, the segmentation decision needs to include both the polarization and magnitude information. Figures 10d and 11d show the results of combining both the magnitude and polarization. In Figure 10d, the dihedral is no longer part of the trihedral. Figure 10c shows the segmentation mainly as a trihedral with a small region that has a lower magnitude. Including the polarization does not add a lot to the segmentation, but the dihedral is better segmented from the trihedral (Figure 10d. When the pixels contain objects with different polarizations, the polarization is decided by the least squares distance described in Section 3.1.

While the magnitude segmenter has no issues in the first two cases and even works fairly well in case 3, it fails on the fourth case. The trihedral and dihedral are segmented as a single region shown in Figure 11c. According to Figure 11e, the trihedral and dihedral have different polarization decisions and segment separately according to the polarization of each. When the image is segmented according to Algorithm 2, the two objects are also segmented separately as seen in Figure 11d. Figure 11d has the trihedral and dihedral separate the same as Figure 11e, but has a higher threshold for which pixels should be included in the segment. In terms of the user-defined thresholds, Figure 11d matches Figure 11c, but the trihedral contains more pixels.

The proposed inclusion of polarization does have limitations to distinguishing between targets. If the two scatterers are of the same polarization, the proposed polarization segmentation gives the same results as the segmentation by magnitude

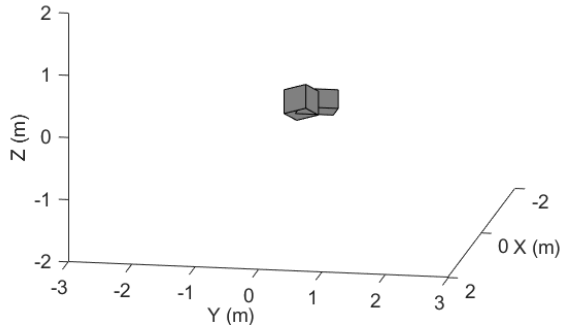

(a) Original scene

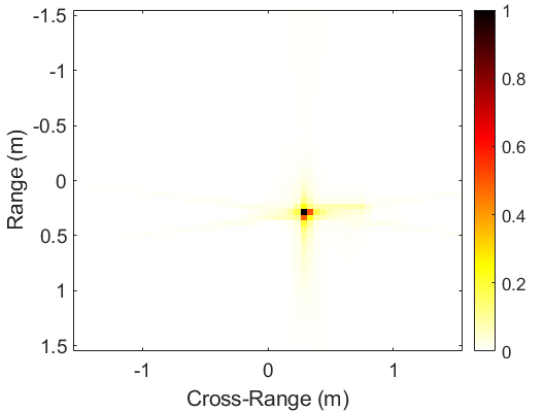

(b) Composite Image

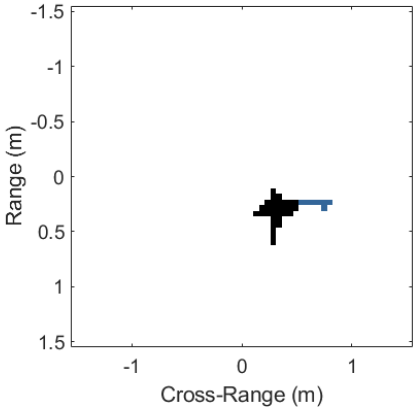

(c) Segmentation by magnitude

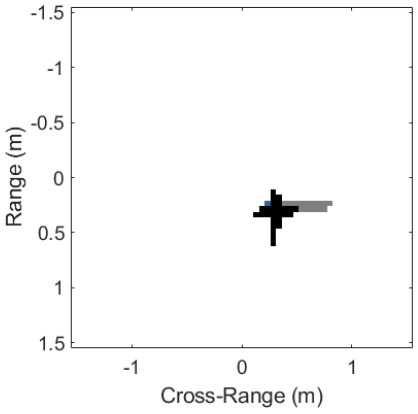

(d) Segmentation by polarization and magnitude

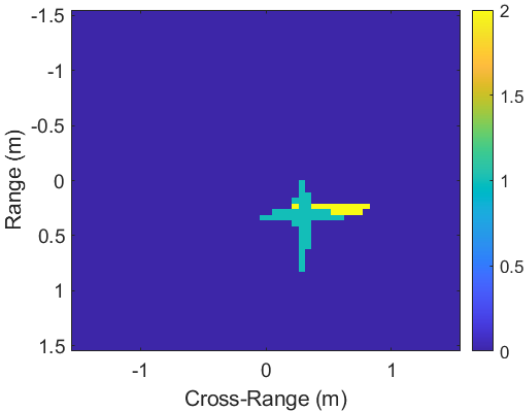

(e) Segmentation by polarization

Figure 10: Case 3 contains a dihedral and a trihedral unresolved in range and cross-range. The scene, the composite SAR image for two full-pol passes, the polarization classification, and the segmentations by Algorithms 1 and 2 are shown.

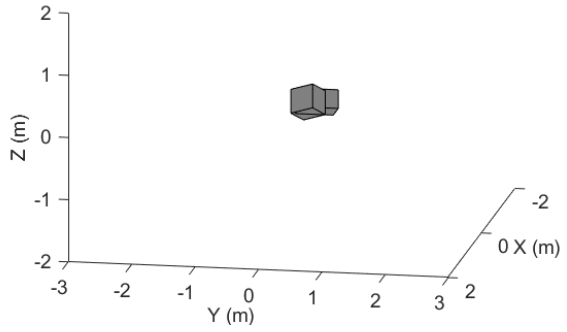

(a) Original scene

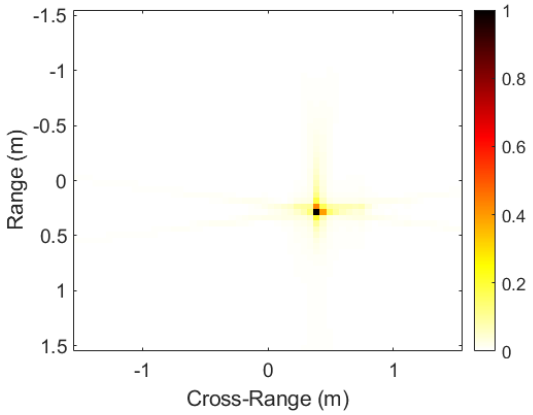

(b) Composite Image

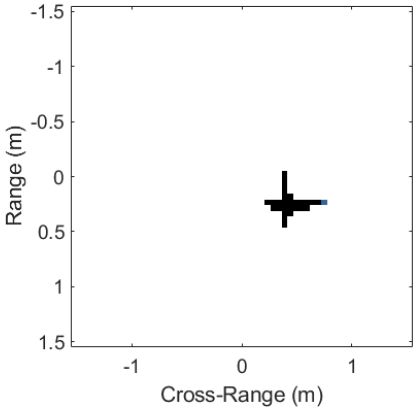

(c) Segmentation by magnitude

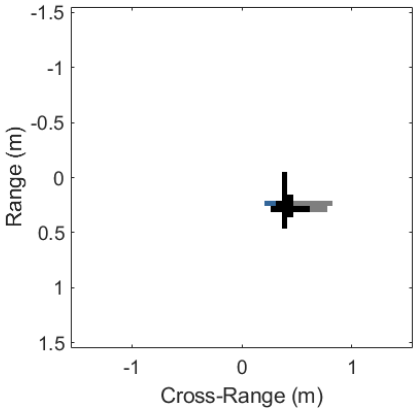

(d) Segmentation by polarization and magnitude

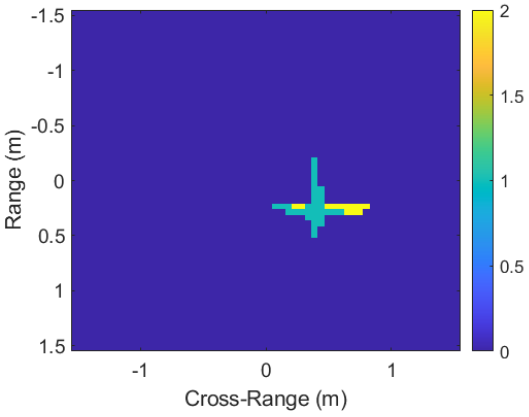

(e) Segmentation by polarization

Figure 11: Case 4 shows a dihedral and a trihedral unresolved in range and cross-range. The scene, the composite SAR image for two full-pol passes, the polarization classification, and the segmentations by Algorithms 1 and 2 are shown.

alone. To demonstrate this, a scene is created involving two dihedrals, which are unresolved in range and cross-range (Figure 12a). The segmented images for this scene are in Figures 12c and 12d. Figures 12c and 12d show that the image has the same segmentation regardless of whether the polarization decision is included or not. Figure 12e also segments the image into a single segment. Since the two dihedrals are placed next to each other and are identical, segmenting them as a single dihedral would still give an accurate representation of the original scene.

Similar to the fifth case, the sixth case has two unresolved objects with the same polarization (Figure 13a). In contrast, the two objects are trihedrals and have an odd polarization instead of an even polarization. Figure 13e shows that all the pixels in the trihedrals are represented by a 1 or odd bounce, whereas Figure 12e has all the pixels in the dihedrals as a 2 which is an even bounce. Figures 13c and 13e distinctly show both trihedrals. The distinction between the trihedrals in Figure 13c is a result of the user-defined threshold. Adding in the polarization does not take away from the magnitude segmentation but rather adds more information to ensure the pixels contained in each segment is as similar as possible. Figure 13d shows the results of combining the information in Figure 13c and Figure 13e.

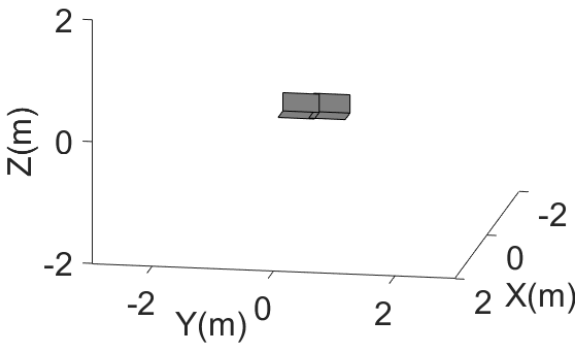

(a) Original scene

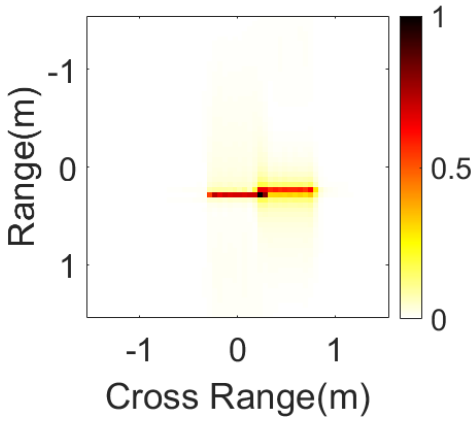

(b) Composite Image

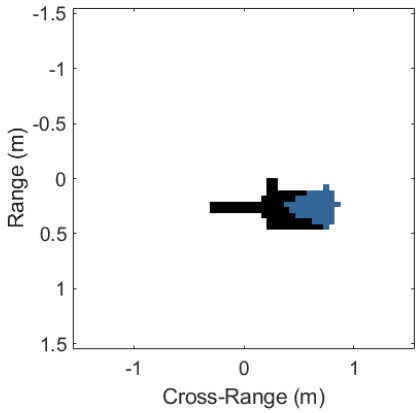

(c) Segmentation by magnitude

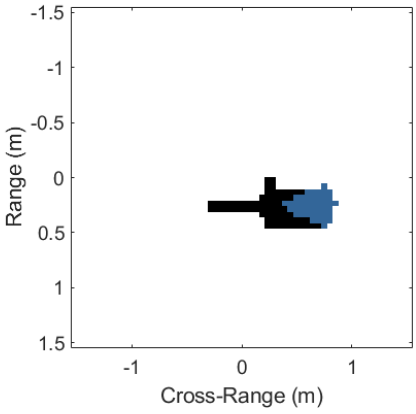

(d) Segmentation by polarization and magnitude

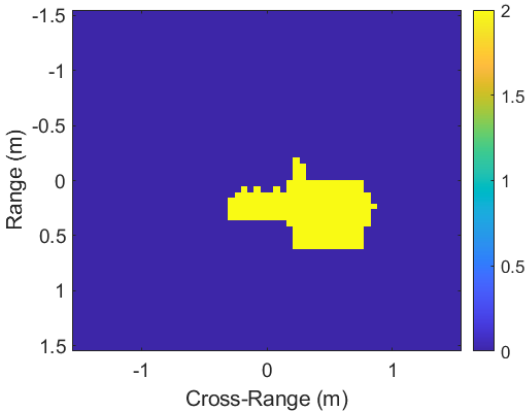

(e) Segmentation by polarization

Figure 12: Simple scene of two dihedrals unresolved in range and cross-range. The scene, the composite SAR image for two full-pol passes, the polarization classification, and the segmentations by Algorithms 1 and 2 are shown.

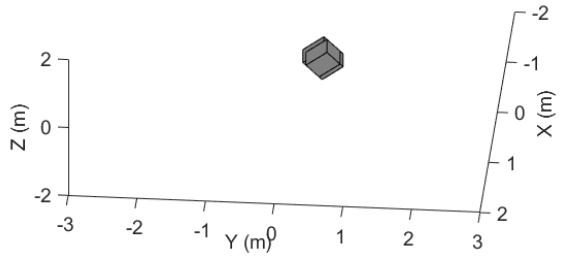

(a) Original scene

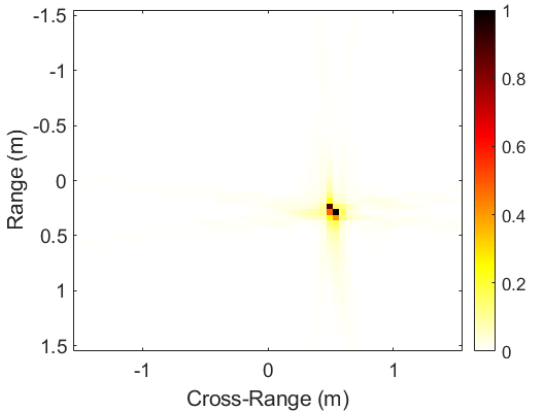

(b) Composite Image

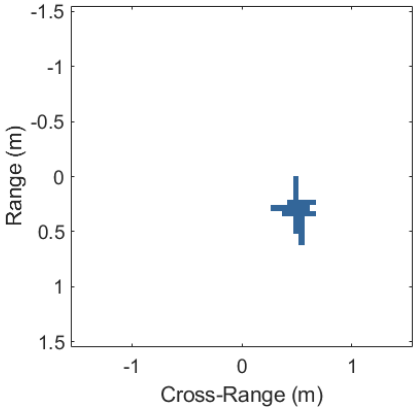

(c) Segmentation by magnitude

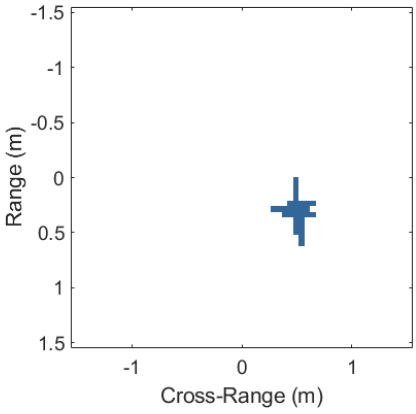

(d) Segmentation by polarization and magnitude

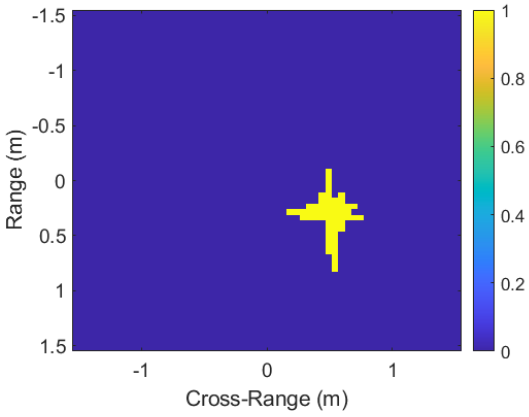

(e) Segmentation by polarization

Figure 13: Simple scene of two trihedrals unresolved in range and cross-range. The scene, the composite SAR image for two full-pol passes, the polarization classification, and the segmentations by Algorithms 1 and 2 are shown.

Finally, the image segmentation algorithms are applied to the backhoe XPatchT data set [1,2,8]. In [1], Algorithm 1 is applied to the backhoe to show its improvements over its predecessor, which did not include region merging. A similar experiment is performed to show the improvement of adding in a polarization decision. The merging criteria in [1] are $p = 1$, $\tau_1 = -4$ dB, $\tau_2 = -15$ dB, $\tau_3 = -25$ dB, and the maximum number of segments is 50. The variable p determines which pixels are considered neighbors to the pixel under test and the three τ's are the various thresholds. The radar parameters for the scene in [1] are given by azimuth $\phi =\in [66°, 114°]$, an elevation $\theta = 30°$, and $SNR = 40$ dB. We use the same merging criteria; however, the radar parameters are changed such that the azimuth angles are matched as closely as possible to the scene in [2]. The radar parameters used are $\phi \in [78.86°, 101.07°]$ and $\theta = 20°$.

The composite image of the backhoe is shown in Figure 14a, which shows how many scatterers are in the scene. Each scatterer is originally segmented separately, but depending whether the image segmentation algorithm includes the polarization decision or not determines how the regions are merged. Figure 14b shows what the segments would look like if the image were segmented only by polarization, while Figure 14c is just segmented by magnitude. Comparing Figures 14b and 14c demonstrates the difference in the two properties. Some segments in Figure 14c are combined into a single region since all the pixels are within the threshold. However, Figure 14b shows these segments as separate since they have different polarizations. Figure 14d combines the two the polarization and magnitude decisions so that regions that do not have the same polarization are left separate. Figure 14d also has regions with the same polarization combined as long as they fall within the magnitude thresholds. Specifically, there is long bright green line in Figure 14d that is broken into four segments in Figure 14c. Conversely, Figure 14c has a large olive green segment that

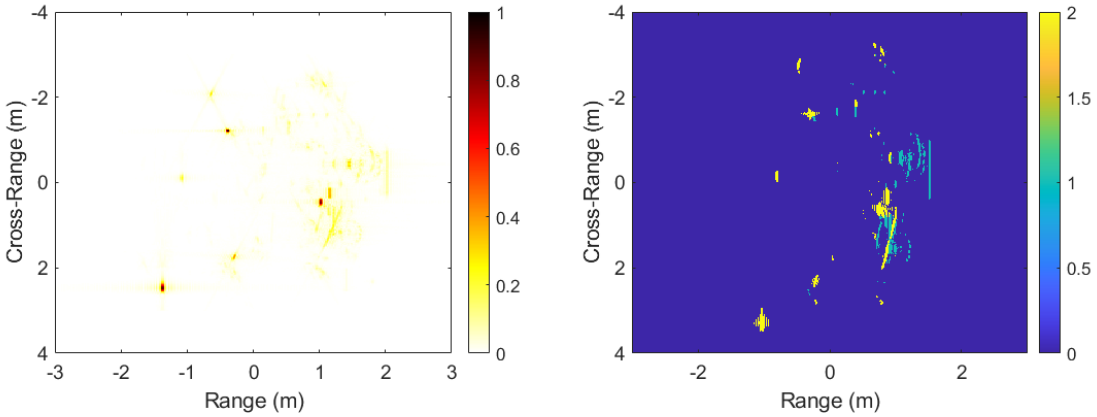

(a) Composite Image

(b) Polarization Decision

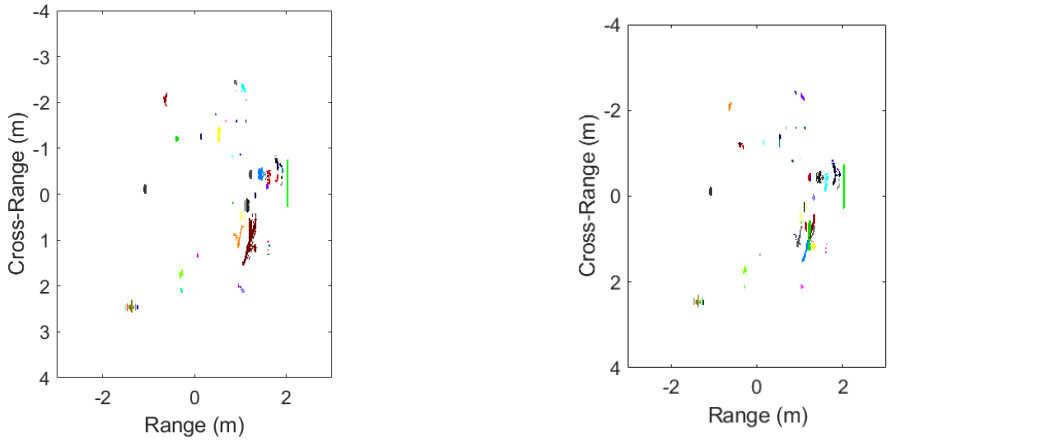

(c) Segmentation by magnitude

(d) Segmentation by polarization and magnitude

Figure 14: Segmented images of a construction backhoe comparing the segmentation by magnitude with the segmentation by polarization and magnitude.

Figure 14b shows has different polarizations. Figure 14d has the segment broken into segments according to polarization. In [2], the segments in the backhoe are classified as canonical shapes to aid in feature extraction. While feature extraction is not included in this thesis, the segments can be more easily classified as their respective canonical shape, since the polarization of the segment is known.

IV. IFSAR Height Estimates

4.1 Preamble

The image segments found in the previous chapter can be used to find the height of the object in the segment using IFSAR. IFSAR looks at the phase difference between a pair of pixels or between a group of pixels from two different images with a slight elevation difference. The groups of pixels for the IFSAR estimates are the image segments from Chapter III.

There are multiple methods to estimate heights, which involve a pair of images with a small difference in elevation angle. The maximum likelihood (ML) estimate from [3] is one way. In [2], two methods of IFSAR processing are explained and compared. The first method in [2], the pixel-by-pixel ML method was previously established, while the least-squares (LS) method was introduced in [2]. The LS method like the ML method can be applied to a single pixel or multiple pixels. Unlike the ML methods, the LS methods requires more than a single polarization channel.

In this chapter, the four height estimators are defined and compared. The mean and variance of each estimator are calculated from a series of Monte Carlo trials of a dihedral in random clutter to determine which estimator gives the most accurate and precise height estimate. The height estimators are applied to single pixels, groups of pixels, pixels from a single polarization, and pixels from all four polarization channels. The naming convention that will be followed throughout this thesis is to use subscripts N and p where N indicates the number of pixels and p indicates how many polarization channels are used. For example, if the ML method is used with a single pixel and data from all four polarization channels, it would be denoted as $ML_{1,4}$. Conversely, if the LS estimator is used with all the pixels in the segments and uses all four polarization channels, it would be denoted as $LS_{N,4}$.

4.2 Methods of IFSAR Processing

4.2.1 Maximum Likelihood Estimate

The ML estimate method from [3], which will be referred to as $ML_{N,1}$ throughout this thesis, is thoroughly described in Section 2.4. However, a summary of the method is included here. Jakowatz' method looks for the ML estimate of the phase difference between the first image, f, and the second image, g. The ML estimate is determined by the complex conjugate, f^*g, and given by

$$\hat{\Psi}_{ML} = \angle\left(\sum_{k=1}^{N} f_k^* g_k\right) \tag{21}$$

which takes the place of Ψ in Equation (12) [3], which is also included here

$$h\left(x,y\right) = \Psi\frac{c}{4\pi f_c\left(\tan\theta_1 - \tan\theta_2\right)\cos\left(\frac{1}{2}\left(\theta_1+\theta_2\right)\right)}. \tag{22}$$

In [3], the ML estimate has to be repeated for each of the polarization channels. After calculating the the ML estimate for each channel, the four values can be averaged to get a single height estimate. The ML estimate can also be applied to all the pixels in all four polarization channels in a segment by stacking the pixels to form a $4N \times 1$ vector if the segment is N pixels. This thesis will refer to the ML estimate for data from a single polarization as $ML_{N,1}$ and as $ML_{N,4}$ for data from all four polarizations. The $ML_{N,1}$ estimator also takes the average of the four height estimates produced by finding the height estimate for each polarization channel.

The pixel-by-pixel method is denoted as $ML_{1,4}$ and is described in [2] and Section 2.4. The $ML_{1,4}$ estimator uses maximum likelihood like $ML_{N,1}$ and $ML_{N,4}$. The $ML_{1,4}$ estimator looks at each pixel in image f or segment f_{seg} and the corresponding pixel in image g or segment $g_{seg}$to form as many pixel pairs as are pixels in one image

or segment. The $ML_{1,4}$ estimator then finds the phase difference in each pixel pair from images f and g. The height estimate is obtained by setting $\Psi = \angle f^* g$ [2] and then using Equation (22). $ML_{1,4}$ returns a matrix of height estimates the same size as the image. We can average across all the height estimates in a given segment to get a single value or take the height of the centroid pixel in the segment. Since the phase difference between pixel pairs varies, $ML_{1,4}$ has a wide variance in the estimates. The process for $ML_{1,4}$ is similar to the process of $ML_{N,1}$ and $ML_{N,4}$ except that it finds the height estimate for each pixel pair rather than a single height for the entire segment.

4.2.2 Least Squares Estimate

In Section 2.4, $LS_{N,4}$ is introduced but is first proposed in [2]. $LS_{N,4}$ finds the least squares fit of the pixels in the segment for each image, f and g using the data from all four polarization channels rather than a single channel. For $LS_{N,4}$, all the pixels in each segment for all polarization channels and stacks them. Thus for a segment with N pixels f_{seg} and g_{seg} are $4N \times 1$ vectors, where f_{seg} and g_{seg} contain the stack of pixels for images f and g respectively. The height of the scattering centers is obtained by taking the least squares fit of f_{seg} and g_{seg} such that the phase term term, Ψ, is instead from [2]

$$\Psi = \angle \left(\left(f_{seg}^H f_{seg} \right)^{-1} f_{seg}^H g_{seg} \right) \tag{23}$$

We then use the Ψ calculated in (23) to determine the height from Equation (22) [2]. Furthermore if Ψ and f_{seg} are known, g_{seg} can be calculated [2] as

$$g_{seg} = \exp\left(j\Psi\right) A_1 f_{seg} \tag{24}$$

Like the ML method, the least squares method can be applied to a single pixel or to the entire segment. For a single pixel, $LS_{1,4}$, f_{seg} and g_{seg} are 4×1 rather than $4N \times 1$. The single pixel is the centroid pixel of the segment. The centroid pixel is found by determining the weighted average of the rows and columns in each segment. The magnitude of the pixel located at the average row-column pair is taken from each polarization channel for both images and placed in f_{seg} and g_{seg} respectively.

Like the ML estimator, the least squares estimator is an unbiased estimator. The two estimators are even equivalent if the following assumptions of the data are met [20]:

- Linearity
- Homoscedasticity or constant variation σ^2
- Normality
- Independence of errors, ε

For these cases, we do not have linearity, since the phase difference between the images is exponential. Thus, the ML estimate and least squares estimate will return different results.

4.3 Comparing the Height Estimates

The methods described above are compared by first re-implementing the experiments described in [2] with the canonical scene. We will not be entirely recreating the experiments and will assume the orientation, size, and shape are already known. Thus, we are only interested in finding the x, y, and z coordinates of each target. To find the x, y-coordinates, the image segments and IFSAR height estimates are used. Since the scene is 3D and the image is 2D, the scatterers layover in the image. The

layover effect causes the x, y-coordinates to be projected in a different location. The segments are from the projected location. The pixels in each segment can be converted to the projected x, y-coordinates in meters. Then, to remove the layover effects, the estimated height is used in Equations (14) and (15). Once the x, y, z-coordinates are estimated, the locations of each scatterer can be plotted.

In [2], the backhoe data set is considered mainly for feature extraction purposes. This thesis will use the same backhoe data, but will focus on the height estimates of the segments from Section 3.2. The x, y-coordinates are also estimated for the backhoe and the results are compared to a CAD model.

4.3.1 Height Estimates of Canonical Scenes

We perform three experiments using the same radar parameters as [2]. The radar parameters are set with a center frequency, $f_c = 10$ GHz; bandwidth, $B = 3$ GHz; azimuth angles, $\phi \in [-8.4°, 8.4°]$; elevation angles, $\theta_1 = 20°$ and $\theta_2 = 20.05°$; and resolution, $\rho = 0.067$ m. First, we replicate the experiment in [2] and create a simple scene consisting of five sufficiently spaced targets shown in Figure 15. The parameters for the simple scene are shown in Table 3. The threshold for merging segments is -35 dB to ensure that objects with varying magnitude merge into a single segment. The resulting height and location estimations are in Table 4. $ML_{N,1}$ for this case refers to the average of the measurements from the single polarization channels.

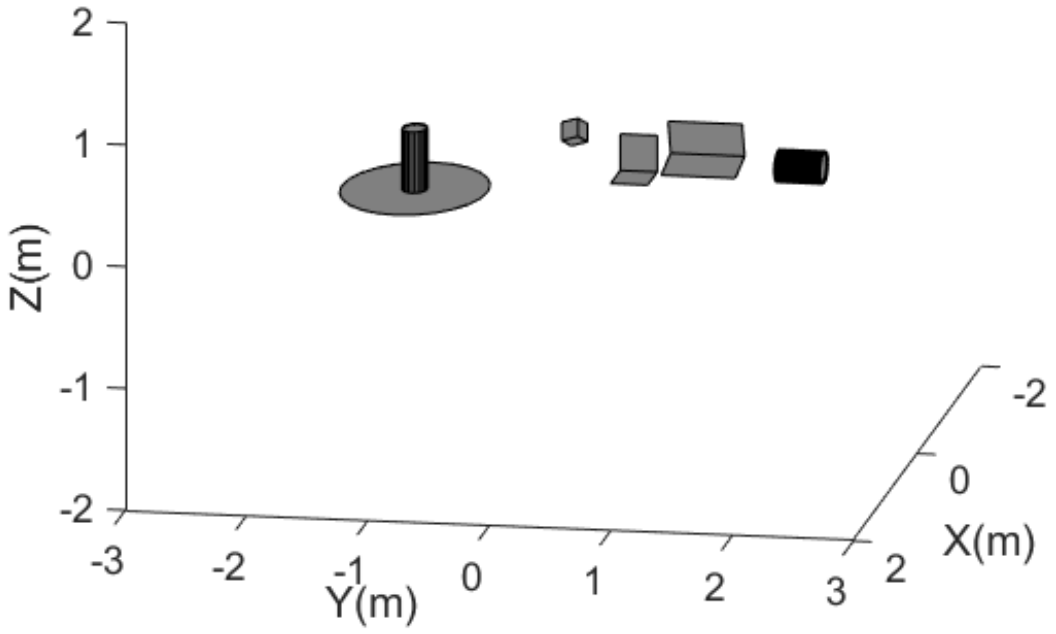

Figure 15: Scene of the five canonical targets used for height estimation.

Table 3: Actual Parameters for the Simple Canonical Scene

shape	x_{true} (m)	y_{true} (m)	z_{true} (m)	$roll_{true}$ (°)	$pitch_{true}$ (°)	L_{true} (m)
Top-hat	0	-1.143	0	—	0	—
Trihedral	-0.762	0	0.2032	20	—	—
Dihedral	-0.254	0.635	0.127	0	0	0.3048
Tilted Dihedral	0	1.27	0.381	0	15	0.6096
Cylinder	-0.508	1.905	0.127	0	—	0.381

Table 4: Estimated Heights for a Single Realization of the Simple Canonical Scene

shape	$z_{ML_{N,1}}$ (m)	$z_{ML_{N,4}}$ (m)	$z_{ML_{1,4}}$ (m)	$z_{LS_{N,4}}$ (m)	$z_{LS_{1,4}}$ (m)	z from [2] (m)
Top-hat	0.0605	1.355e-4	0.3769	1.3558e-4	3.5238e-4	1.27e-5
Trihedral	0.1162	0.2072	0.1285	0.2072	0.32128	0.2042
Dihedral	0.1282	0.1286	0.1150	0.1286	0.1241	0.129
Tilted Dihedral	0.3845	0.3863	0.1644	0.3863	0.3844	0.3828
Cylinder	0.1727	0.1717	0.1308	0.1717	0.1789	0.170

With the exception of the cylinder, $ML_{1,4}$ consistently performs the worst of the height estimators. The $ML_{N,4}$ and $LS_{N,4}$ estimators have approximately the same performance for all the shapes. The Methods $ML_{N,1}$ and $LS_{1,4}$ have similar performance to $ML_{N,4}$ and $LS_{N,4}$ except for the top-hat and trihedral respectively. The $ML_{N,4}$ and $LS_{N,4}$ estimators perform much better in those cases. Additionally, $LS_{N,4}$ is very close to the estimates given in [2]. The slight differences may result from the use of a Taylor window in [2]. To evaluate the x, y-coordinate estimate, Figure 16 shows the estimated versus actual positions. With the exception of the cylinder, the estimated x, y-coordinates are fairly close to where the scatterers were projected into the image.

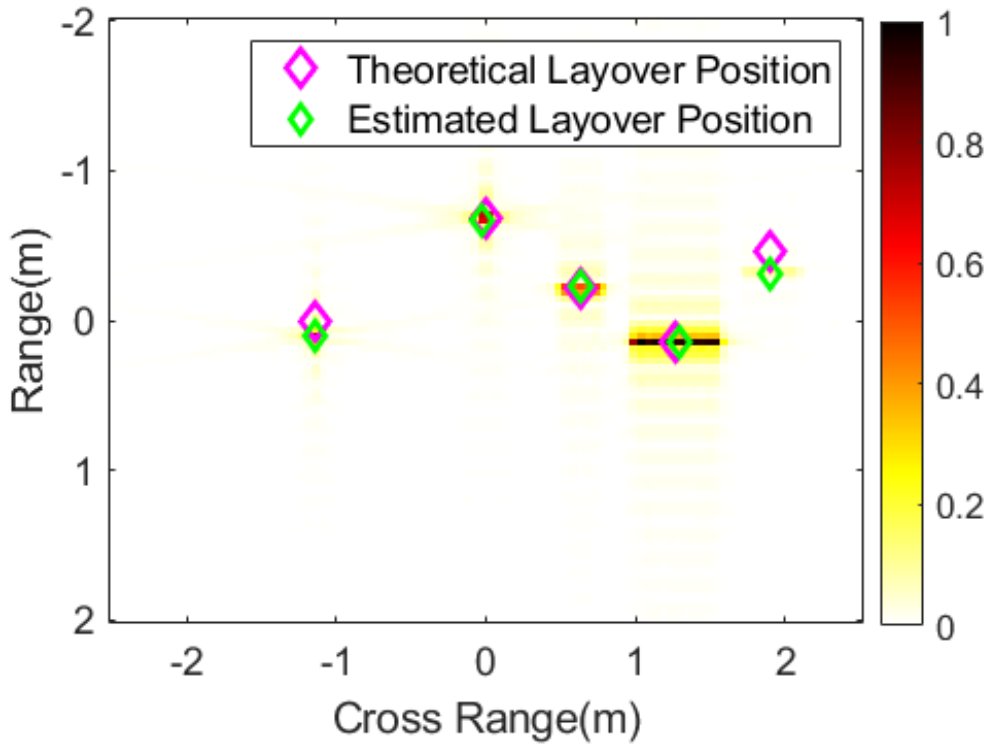

Figure 16: Estimated layover position of canonical shapes versus theoretical layover positions.

The second experiment also follows [2]. We create a dihedral that is 0.91 m long, 0.30 m tall, and placed at $(x, y, z) = (0, 0, 0.635)$ m. The dihedral is placed in a cluttered scene, Figure 17, where the SCR is 40dB and the threshold to merge regions is -20 dB. We perform 100 Monte Carlo trials with random clutter for each trial and compare the performance of the five height estimation methods proposed [2]. These five heights methods are compared in Figures 18a-18c. They are evaluated based on their mean and variance to determine which method performs the best in the presence of clutter. Figures 18a and 18b have the height estimates from $ML_{N,1}$ and $ML_{N,4}$. They show the difference between using only a single polarization versus using fully polarized data. Figure 18c contains $ML_{1,4}$, which is evaluated in its own histogram,

since it has a very wide variance. Figures 18d and 18e contains $LS_{N,4}$ and $LS_{1,4}$. All figures also include the true height value shown by a vertical line.

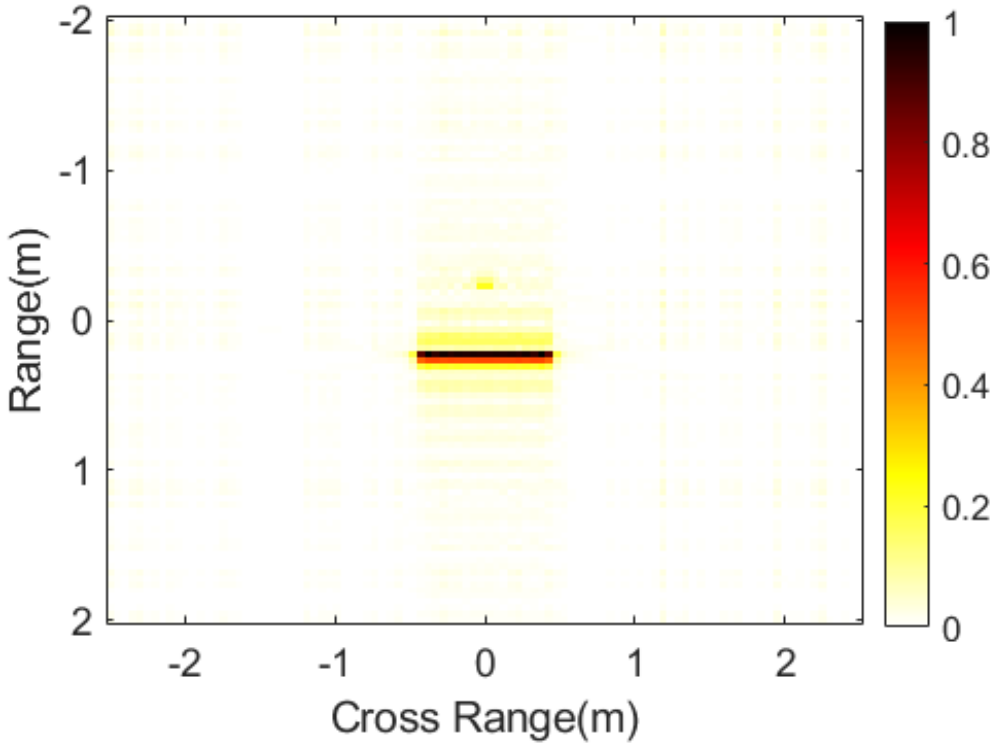

Figure 17: Composite image of a dihedral with clutter that has SCR of 40dB and $\tau_1 = -1$ dB, $\tau_2 = -25$ dB, and $\tau_3 = -20$ dB.

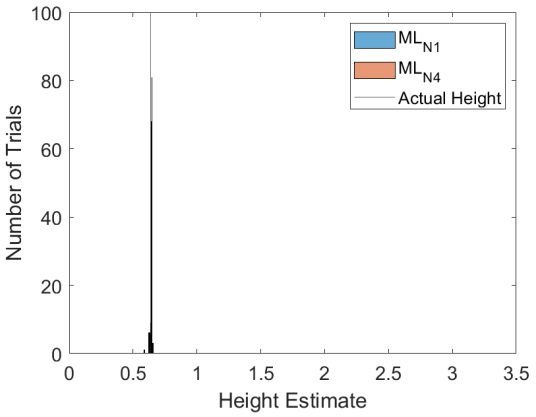

(a) Histogram of $ML_{N,1}$ and $ML_{N,4}$

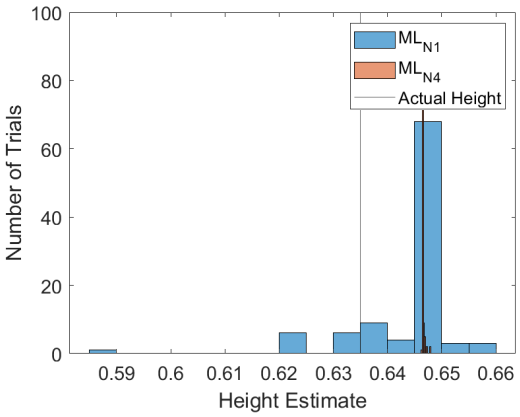

(b) Close up of the Histogram of $ML_{N,1}$ and $ML_{N,4}$

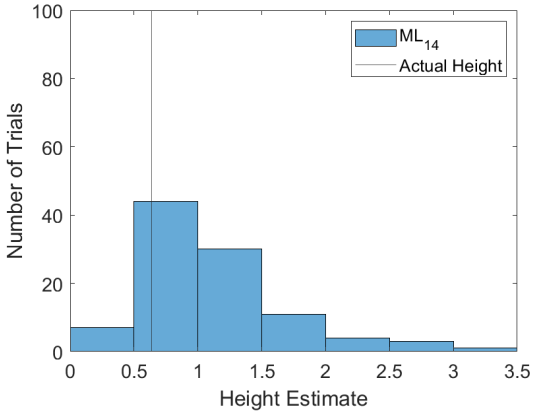

(c) Histogram of $ML_{1,4}$

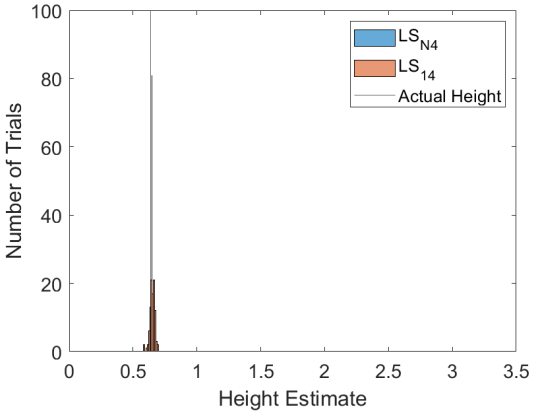

(d) Histogram of $LS_{N,4}$ and $LS_{1,4}$

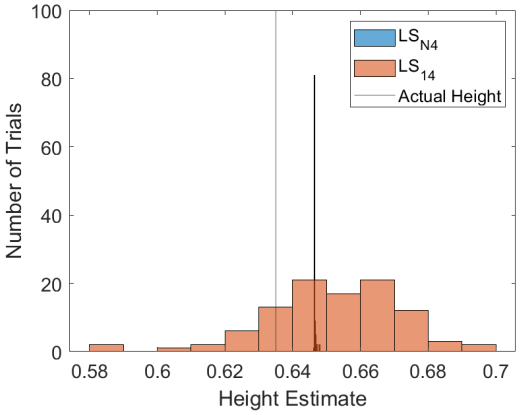

(e) Close up of the Histogram of $LS_{N,4}$ and $LS_{1,4}$

Figure 18: Histogram of the height estimators showing each methods mean and variance. The values for the mean and variance are quantified in Table 5.

Table 5: Variance and Mean for Height Estimates

Method	Mean (m)	Variance (m)	Z (m)
$ML_{N,1}$ for HH	0.6433	3.3331e-7	0.635
$ML_{N,1}$ for HV	0.6107	3.9349e-4	0.635
$ML_{N,1}$ for VH	0.6689	0.0018	0.635
$ML_{N,1}$ for VV	0.6500	4.8705e-7	0.635
$ML_{N,1}$ Average across Channels	0.6432	8.5606e-5	0.635
$ML_{N,4}$	0.6466	4.7294e-8	0.635
$ML_{1,4}$	1.1181	0.3508	0.635
$LS_{N,4}$	0.6466	4.7294e-8	0.635
$LS_{1,4}$	0.6521	3.9493e-4	0.635

In the presence of noise, $ML_{N,4}$ and $LS_{N,4}$ have the same performance. If only variance is considered, $ML_{N,4}$ and $LS_{N,4}$ perform the best followed by $ML_{N,1}$, $LS_{1,4}$, and $ML_{1,4}$ performs the worst. In terms of mean, $ML_{N,1}$ performs the best followed by $ML_{N,4}$ and $LS_{N,4}$ and then $LS_{1,4}$. Again the worst performer is $ML_{1,4}$. Without noise, the best estimators on average are $ML_{N,4}$ and $LS_{1,4}$. Even though $ML_{N,4}$ and $LS_{N,4}$ are the second best estimator for the mean in the presence of noise, they overall provide the most accurate and precise height estimate. The two methods have the lowest variance with noise, have a mean value that is approximately 1 cm from the true value with noise, and generally provide the most accurate measurement without noise. The second best estimator is $ML_{N,1}$ although it does provide slightly better results in the presence of noise. The difference in mean between $LS_{N,4}$, $ML_{N,4}$, and $ML_{N,1}$ is 0.0034 m, which gives $ML_{N,1}$ an error of 0.0082 m and $ML_{N,4}$ and $LS_{N,4}$ an error of 0.0116 m. In noise, $ML_{N,1}$ is slightly more accurate, but $ML_{N,4}$ and $LS_{N,4}$

are more precise. Considering that $ML_{N,4}$ and $LS_{N,4}$ perform better without noise, they are overall the best estimators.

4.3.2 Backhoe Data

The IFSAR methods can also be applied to simulated scenes containing objects other than the canonical models. For example, we can use IFSAR to determine the height of a backhoe. The backhoe used is from the XPatchT data set [2], [8]. The backhoe data set has a center frequency of $10GHz$ and covers the range of frequencies from $7GHz$ to $10GHz$ [2], [8], [21]. The data set contains the full polarization and covers the full 360° in azimuth while the elevation ranges from 0° to 90° with 0.05° between spacing between elevations [2], [8], [21].

In [2], the broadside view and front view of the backhoe are considered. The elevation pair chosen in [2] are $\theta_1 = 30^\circ$ and $\theta_2 = 30.05^\circ$ while the azimuth range is $\phi \in [78.83^\circ, 101.11^\circ]$ for the broadside view and $\phi \in [78.83^\circ, 101.11^\circ]$ for the front view. While [2] focuses on feature extraction for the backhoe, we focus on the height estimate and use the canonical models estimating the backhoe in [2] to perform the height estimates.

We only consider the broadside of the backhoe (Figure 19a) at an elevation pair of $\theta_1 = 20^\circ$ and $\theta_2 = 20.05^\circ$. Figure 19a depicts the CAD model of the backhoe taken from the broadside view such that $\phi \in [79^\circ, 100^\circ]$. The CAD model is given in inches, so the location estimates are also given in inches. Since for the canonical shapes $ML_{N,4}$ and $LS_{N,4}$ were the best estimators, Figure 19a shows the height estimates for each segment. In Figure 19a, the blue circles are for $ML_{N,4}$ and the red pluses are for $LS_{N,4}$. From the image, the height estimates are fairly close to the backhoe's height. Many of the estimated x, y-coordinates fall on the CAD model fairly well (Figure 19b), but there are a few estimates that do not fall on the CAD model. The

location estimates are also calculated for both segmenters to compare the performance of Algorithm 1 and Algorithm 2 shown in Figure 20a and 20b. The $LS_{N,4}$ height estimator is used with both algorithms. The layover effects in Figures 20a and 20b are removed with the corresponding IFSAR height estimate.

Both segmenters give the same location estimates for the roof segment and are off by only a small height. While Algorithm 2 does not improve the estimates for the backhoe roof segment, Algorithm 2 does improve the estimates of other high energy regions. For example,Algorithm 2 improves the estimates along the loader arm. In the loader arm, Algorithm 2 provides estimates for the lift arm and the cylinder, while Algorithm 1 segments both objects as a single object located halfway between the two objects. The performance of the two segmenters is further compared in the next section.

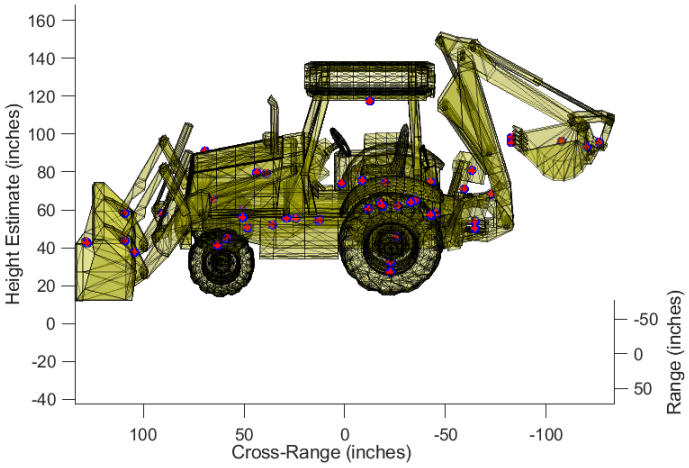

(a) Backhoe CAD Model with Height Estimates

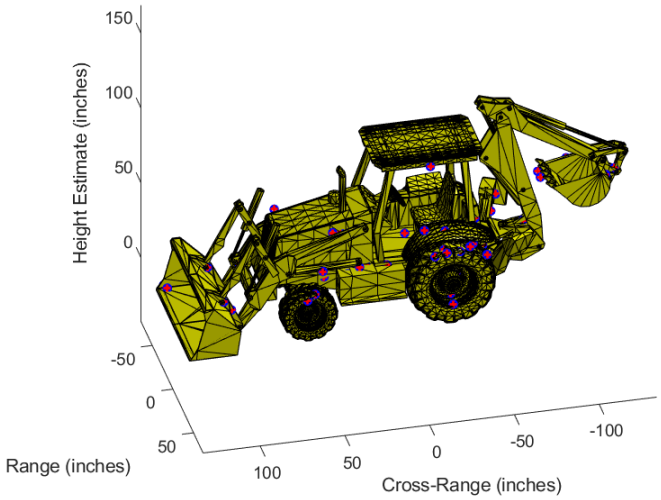

(b) Rotated Backhoe CAD Model with Height Estimates

Figure 19: CAD model of the broadside of a backhoe overlaid with the estimated x, y, z-coordinates. The x, y, z-coordinates describe the backhoe in 3D, so the backhoe is rotated to show how the estimated points lay on the CAD model.

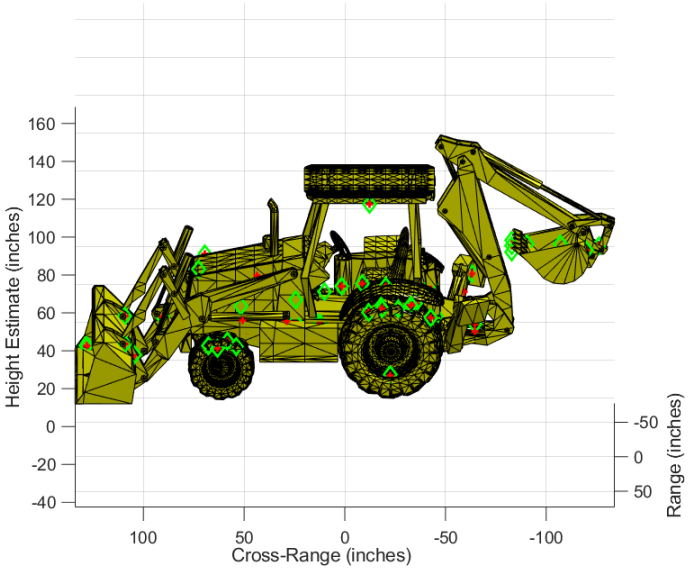

(a) Backhoe CAD Model with Roof Height Estimates

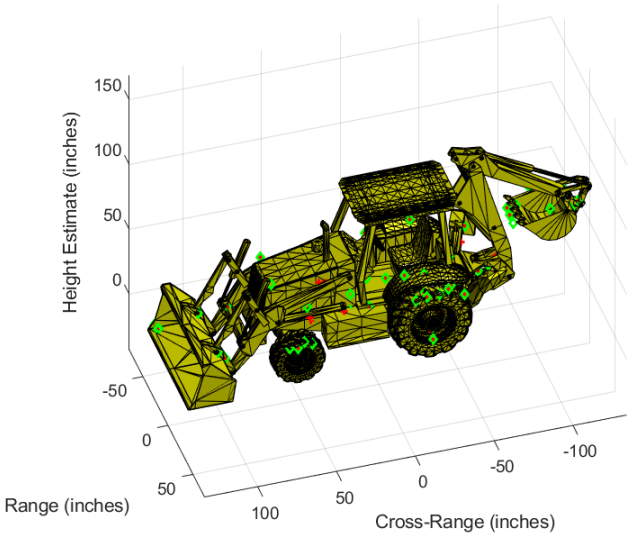

(b) Rotated Backhoe CAD Model with Roof Height Estimates

Figure 20: CAD model of the broadside of a backhoe overlaid with the estimated x, y, z-coordinates from both segmentation algorithms. The red pluses represent the estimates using Algorithm 2 and the green diamond represents the estimates from Algorithm 1. $LS_{N,4}$ is used for the z-coordinate.

4.3.3 Height Estimates from Image Segmentation Algorithm 2

Finally, a scene is created with a trihedral and dihedral similar to the scenes created in Section 3.2. In this case, the trihedral is set at $x = -1.5199$ m, $y = 0.2$ m, and $z = 5$ m, so that when it lays over in the image it is unresolved with the dihedral, which is set at $x = 0.25$ m, $y = 0.5$ m, and $z = 0$ m. The thresholds are set to $\tau_1 = -4$ dB, $\tau_2 = -25$ dB, and $\tau_3 = -30$ dB. With Algorithm 1, the thrihedral and dihedral are segmented together (Figure 21d) resulting in a single height estimate instead of a height estimate for each object. Figure 21c shows what happens when a radar image is taken of the scene in Figures 21a and 21b. In the polarization decision (Figure 21f), the pixels of the trihedral are mixed with the pixels of the dihedral though Figure 21f still shows two main groups of pixels. When using Algorithm 2, the trihedral and dihedral are segmented into five different segments according to the thresholds and the polarization decision (Figure 21e. The two highest energy segments in Figure 21e are the mainlobes of the trihedral and dihedral. Table 6 only includes the IFSAR heights for the first two segments, which are the mainlobes of the trihedral and dihedral.

Using the segmentation from Algorithm 1, a single IFSAR height is estimated placing both objects around 5 m. Having both objects classified as a trihedral at $z = 5$ m would inaccurately represent the imaged scene shown in Figures 21a and 21b. From Algorithm 2, the trihedral and dihedral are given an IFSAR height estimate for each object. The results of both algorithms are given in Table 6 for the first two segments in Figure 21e. The first two segments in Figure 21e are the large black segment corresponding to the trihedral's mainlobe and the largest, dark grey segment corresponding to the dihedral's mainlobe. Including multiple pixels at a single polarization for the trihedral returns 5.0697 m and 5.0374 m in the HH and VV channels respectively. However, since the trihedral does not appear in the HV

and VH channels, the results are near zero. The $ML_{N,1}$ result in Table 6 is the average of the heights estimated in all four channels. For the dihedral, none of the IFSAR estimators perform well for Algorithm 2, but the estimates clearly show the objects at a different z-coordinate than IFSAR performed on segments from Algorithm 1. Some of the error in the dihedral is a result of the pixels from the trihedral mixing with the dihedral. In Figure 21f, the trihedral is broken into three segments surrounding the dihedral; the dihedral is broken into two with one of its pixels inside the trihedral segment. If more of the dihedral were present in the segment, the height estimate for the dihedral would improve.

Table 6: IFSAR Heights for Algorithms 1 and 2

Algorithm	Segment	$ML_{1,4}$ (m)	$ML_{N,1}$ (m)	$ML_{N,4}$ (m)	$LS_{1,4}$ (m)	$LS_{N,4}$ (m)
1	1	2.5472	2.4951	4.9875	5.0244	4.9875
2	1	2.5472	2.5270	5.0534	5.0821	5.0534
2	2	0.7783	0.3219	0.6422	0.6890	0.6422

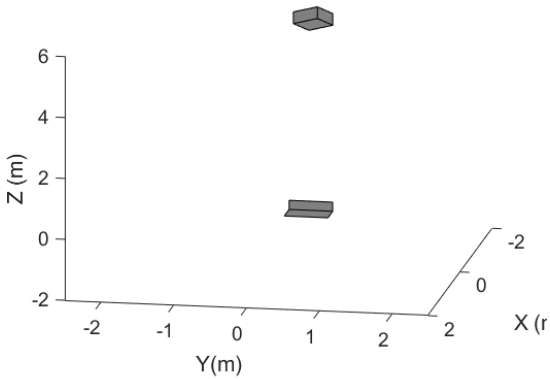

(a) IFSAR Image 1 at $\theta = 20°$

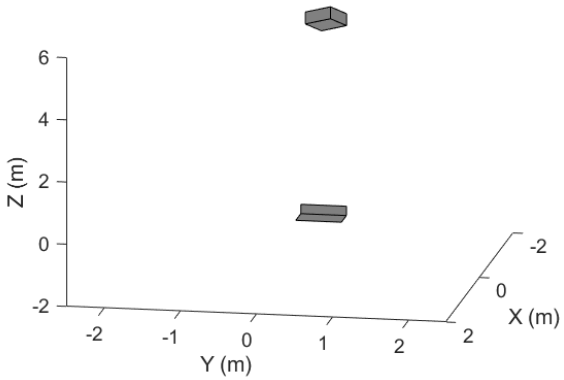

(b) IFSAR Image 2 at $\theta = 20.05°$

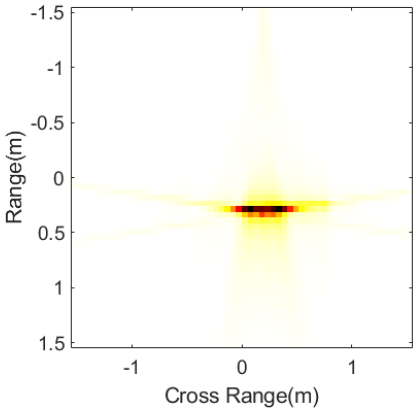

(c) Composite Image

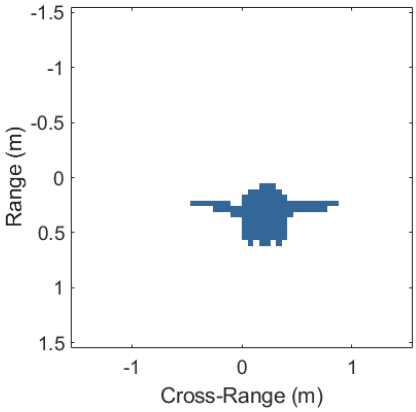

(d) Segmentation with Algorithm 1

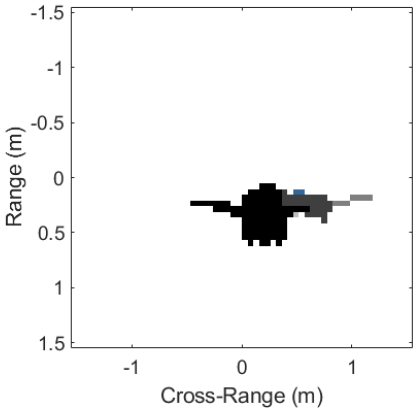

(e) Segmentation with Algorithm 2

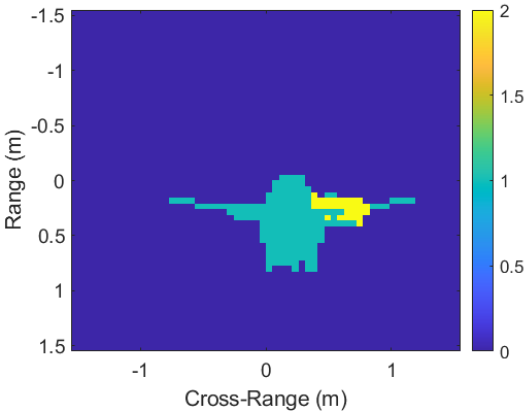

(f) Polarization Decision

Figure 21: IFSAR image pair segmented with Algorithms 1 and 2 to find the estimated z-coordinate with IFSAR height estimates.

V. Conclusions

This thesis adds a polarization decision to the image segmentation algorithm, Algorithm 1, in [2]. The resulting algorithm, Algorithm 2, is compared to Algorithm 1 for six different cases to show the benefits of including a polarization decision. This thesis also compares several different height estimators to determine which gave the most accurate and precise results.

Comparing the results from the image segmentation algorithms show the impact of adding in a polarization decision. Checking the polarization allows scatterers that would normally be segmented together to be segmented separately if they differ by polarization. In the case of the trihedral and dihedral scenes, the two would have originally been segmented as a single object. Instead the two objects are segmented as two distinct objects. If feature extraction were performed on the segmented image, the trihedral and dihedral would both be present. When the scene is reconstructed, it would contain both the trihedral and dihedral that were present in the original scene making the reconstruction more accurate. Both image segmentation algorithms were also applied to the backhoe data.

We then used the segmented images to obtain the IFSAR height estimates using five different height estimators. The most accurate and precise estimators on the canonical shapes are $ML_{N,4}$ and $LS_{N,4}$ or the ML estimate from [3] using data from all four polarization channels and the least squares estimate from [2]. We also applied the estimators to the backhoe data. The estimators with the exception of $ML_{1,4}$ provided consistent results of the heights of each segment. The backhoe results show that the estimators can be applied to measured data. Furthermore, the IFSAR estimates improve with the quality of data the estimators are applied to. The polarization decision included in Algorithm 2 improves the quality of data in each segment as shown in the case with the trihedral at height 5 m and the dihedral at height 0 m.

Not only does Algorithm 2 improve the representation of the objects in the imaged scene, but Algorithm 2 also provides better quality data to give more accurate IFSAR height estimates.

Future applications of the IFSAR height estimates is to measure the height of the GOTCHA data set [22] and compare the height estimates to Cloude's fully polarized IFSAR estimates [12].

Bibliography

1. J. Jackson, "Automated image segmentation for synthetic aperture radar feature extraction," *Proceedings of the IEEE 2010 National Aeorspace & Electronics Conference*, pp. 45–49, 2010.

2. J. Jackson and R. Moses, "Feature Extraction Algorithm for 3D Scene Modeling and Visualization Using Monostatic SAR," in *Algorithms for Synthetic Aperture Radar Imagery XIII*, E. G. Zelnio and F. D. Garber, Eds., vol. 6237. SPIE, 2006, pp. 623 708–1–623 708–12.

3. C. Jakowatz, D. Wahl, P. Eichel, D. Ghiglia, and P. Thompson, *Spot-light Mode Synthentic Aperture Radar: A Signal Processing Approach.* New York, NY: Springer Science+Business Media, Inc., 1996.

4. J. Jackson and R. Moses, "Synthetic aperture radar 3D feature extraction for arbitrary flight paths," *IEEE Transactions on Aerospace and Electronic Systems*, vol. 48, no. 3, pp. 2065–2083, 2012.

5. J. Jackson, B. Rigling, and R. Moses, "Canonical scattering feature models for 3D and bistatic SAR," *IEEE Transactions on Aerospace and Electronic Systems*, vol. 46, no. 2, pp. 525–541, 2010.

6. H. Mott, *Remote Sensing with Polarimetric Radar.* Hoboken, NJ: John Wiley and Sons, Inc., 2007.

7. M. Saville, J. Jackson, and D. Fuller, "Rethinking vehicle classification with wide-angle polarimetric sar," *IEEE A & E Systems Magazine*, pp. 41–49, 2014.

8. C. Austin and R. Moses, "Interferometric Synthetic Aperture Radar Detection and Estimation Based 3D Image Construction," in *Algorithms for Synthetic Aper-*

ture Radar Imagery XIII, E. G. Zelnio and F. D. Garber, Eds., vol. 6237. SPIE, 2006, pp. 623 707–1–623 707–12.

9. X. Mao, X. Xiao, and Y. Lu, "PolSAR data-based land cover classification using dual-channel watershed region-merging segmentation and bagging-elm," *IEEE Geoscience and Remote Sensing Letters*, vol. 19, pp. 525–541, 2022.

10. P. Yu, A. Qin, and D. Clausi, "Unsupervised polarimetric SAR image segmentation and classification using region growing with edge penalty," *IEEE Transactions on Geoscience and Remote Sensing*, vol. 50, no. 4, pp. 1302–1316, 2012.

11. Y. Yu and S. Acton, "Polarimetric SAR image segmentation using texture partitioning and statistical analysis," *Proceedings 2000 International Conference on Image Processing*, vol. 1, pp. 677–680, 2000.

12. S. Cloude and K. Papathanassiou, "Polarimetric SAR interferometry," *IEEE Transactions on Geoscience and Remote Sensing*, vol. 36, no. 5, pp. 1551–1565, 1998.

13. Y. Zhang, J. Zhang, G. Huang, and Z. Zhao, "Object-oriented classification of polarimetric SAR imagery based on texture features," *2011 International Symposium on Image and Data Fusion*, pp. 1–4, 2011.

14. J. Ni, F. Zhang, F. Ma, Q. Yin, and D. Xiang, "Random region matting for the high-resolution PolSAR image semantic segmentation," *IEEE Journal of Selected Topics in Applied Earth Observations and Remote Sensing*, vol. 14, pp. 3040–3050, 2021.

15. F. Wang, L. Wu, Q. Zhang, W. Zhao, M. Li, and G. Liao, "Unsupervised SAR image segmentation using higher order neighborhood-based triplet markov fields

model," *IEEE Transactions on Geoscience and Remote Sensing*, vol. 52, no. 8, pp. 5193–5205, 2014.

16. X. Yang, X. Gao, D. Tao, X. Li, and J. Li, *IEEE Transactions on Image Processing.*

17. W. Yang, X. Zhang, L. Chen, and H. Sun, "Semantic segmentation of polarimetric SAR imagery using conditional random fields," *2010 IEEE Transactions on Geoscience and Remote Sensing Symposium*, pp. 1593–1596, 2010.

18. P. Zhang, M. Li, Y. Wu, and H. Li, "Hierarchical conditional random fields model for semisupervised SAR image segmentation," *IEEE Transactions on Geoscience and Remote Sensing*, vol. 53, no. 9, pp. 4933–4951, 2015.

19. K. Ersahin, I. Cumming, and R. Ward, "Segmentation and classification of polarimetric SAR data using spectral graph partitioning," *IEEE Transactions on Geoscience and Remote Sensing*, vol. 48, no. 1, pp. 164–174, 2010.

20. E. García-Portugués, *Notes for Predictive Modeling*, 2022, version 5.9.9. ISBN 978-84-09-29679-8. [Online]. Available: https://bookdown.org/egarpor/PM-UC3M/

21. K. Naidu and L. Lin, "Data dome: full k-space sampling data for high-frequency radar research," in *Algorithms for Synthetic Aperture Radar Imagery XI*, E. G. Zelnio and F. D. Garber, Eds., vol. 5427. SPIE, 2004.

22. C. Casteel and L. G. et al., "GOTCHA Challenge problem," in *Algorithms for Synthetic Aperture Radar Imagery XIV*, E. G. Zelnio and F. D. Garber, Eds., vol. 6568. SPIE, 2007.

REPORT DOCUMENTATION PAGE

Form Approved
OMB No. 0704–0188

1. REPORT DATE *(DD–MM–YYYY)*	2. REPORT TYPE	3. DATES COVERED *(From — To)*
16–06–2022	Master's Thesis	Sept 2020 — Jun 2022

4. TITLE AND SUBTITLE

Polarization-Based Image Segmentation and Height Estimation for Interferometric SAR

5a. CONTRACT NUMBER

5b. GRANT NUMBER

5c. PROGRAM ELEMENT NUMBER

6. AUTHOR(S)

Augusta J. Vande Hey

5d. PROJECT NUMBER

5e. TASK NUMBER

5f. WORK UNIT NUMBER

7. PERFORMING ORGANIZATION NAME(S) AND ADDRESS(ES)

Air Force Institute of Technology
Graduate School of Engineering and Management (AFIT/EN)
2950 Hobson Way
WPAFB OH 45433-7765

8. PERFORMING ORGANIZATION REPORT NUMBER

AFIT-ENG-MS-22-J-016

9. SPONSORING / MONITORING AGENCY NAME(S) AND ADDRESS(ES)

Lincoln Laboratory/Massachusetts Institute of Technology
244 Wood Street
Lexington, MA 02421-6426
COMM 781-981-3455
Email: blejer@ll.mit.edu

10. SPONSOR/MONITOR'S ACRONYM(S)

MIT

11. SPONSOR/MONITOR'S REPORT NUMBER(S)

12. DISTRIBUTION / AVAILABILITY STATEMENT

DISTRIBUTION STATEMENT A:
APPROVED FOR PUBLIC RELEASE; DISTRIBUTION UNLIMITED.

13. SUPPLEMENTARY NOTES

14. ABSTRACT

To find scatterers in a synthetic aperture radar (SAR) image, a modification is proposed to improve peak region segmentation (PRS) with region merging. The modification considers the polarization of each pixel before it is added to a segment to ensure the segment only contains pixels of the same polarization. Prior to region merging, the polarization of the segments is compared, so that only segments with the same polarization are merged into a single region. The segmented regions are used to find the height of each scatterer through interferometric SAR (IFSAR) processing. Multiple methods of IFSAR are examined to find the best height estimator. The best height results come from using all the pixels in the segment from all four polarization channels.

15. SUBJECT TERMS

SAR, IFSAR, Fully-Polarimetric Data

16. SECURITY CLASSIFICATION OF:			17. LIMITATION OF ABSTRACT	18. NUMBER OF PAGES	19a. NAME OF RESPONSIBLE PERSON
a. REPORT	b. ABSTRACT	c. THIS PAGE			2d Lt Augusta J. Vande Hey, AFIT/ENG
U	U	U	UU	72	19b. TELEPHONE NUMBER *(include area code)* (608) 485-2189; augusta.vandehey@afit.edu